Paleoceanography and Paleoclimatology

AGU ADVANCING EARTH AND SPACE SCIENCE

RESEARCH ARTICLE
10.1029/2021PA004294

Neogene Mass Accumulation Rate of Carbonate Sediment Across Northern Zealandia, Tasman Sea, Southwest Pacific

R. Sutherland[1], Z. Dos Santos[1], C. Agnini[2], L. Alegret[3], A. R. Lam[4,5], T. Westerhold[6], M. K. Drake[7], D. T. Harper[8], E. Dallanave[6], C. Newsam[9], M. J. Cramwinckel[10], G. R. Dickens[11], J. Collot[12], S. J. G. Etienne[12], A. Bordenave[12], W. R. Stratford[13], X. Zhou[14], H. Li[15], and G. Asatryan[16]

[1]SGEES, Victoria University of Wellington, Wellington, New Zealand, [2]Dipartimento di Geoscienze, Università di Padova, Padova, Italy, [3]Departamento de Ciencias de la Tierra, Universidad de Zaragoza, Zaragoza, Spain, [4]University of Massachusetts Amherst, Amherst, MA, USA, [5]Department of Geology, Binghamton University, Binghamton, NY, USA, [6]'Geosciences' for Dallanave; and MARUM for Westerhold, University of Bremen, Bremen, Germany, [7]Department of Ocean Sciences, University of California, Santa Cruz, CA, USA, [8]Department of Geology, University of Kansas, Lawrence, KS, USA, [9]Earth Sciences, University College London, London, UK, [10]Ocean and Earth Science, National Oceanography Centre, University of Southampton, Southampton, UK, [11]Department of Geology, Trinity College Dublin, Dublin, Ireland, [12]Geological Survey of New Caledonia, DIMENC, Noumea, New Caledonia, [13]GNS Science, Lower Hutt, New Zealand, [14]Environmental & Biological Sciences, Rutgers, The State University of New Jersey, New Brunswick, NJ, USA, [15]Institute of Oceanology, Chinese Academy of Sciences, Qingdao, China, [16]Museum für Naturkunde, Leibniz-Institut für Evolutions und Biodiversitätsforschung, Berlin, Germany

Key Points:

- Marine carbonate productivity in Tasman Sea varied by a factor of 3–5 since 25 Ma
- Peak Neogene productivity was at 7–5 Ma and was more than double that since 2 Ma
- Currents and gravity flows resulted in high spatial variability of mass accumulation rate

Supporting Information:

Supporting Information may be found in the online version of this article.

Correspondence to:

R. Sutherland,
rupert.sutherland@vuw.ac.nz

Citation:

Sutherland, R., Dos Santos, Z., Agnini, C., Alegret, L., Lam, A. R., Westerhold, T., et al. (2022). Neogene mass accumulation rate of carbonate sediment across northern Zealandia, Tasman Sea, southwest Pacific. *Paleoceanography and Paleoclimatology*, *37*, e2021PA004294. https://doi.org/10.1029/2021PA004294

Received 4 MAY 2021
Accepted 4 JAN 2022

Author Contributions:

Conceptualization: R. Sutherland
Investigation: R. Sutherland, Z. Dos Santos, C. Agnini, L. Alegret, A. R. Lam, T. Westerhold, M. K. Drake, D. T. Harper, E. Dallanave, C. Newsam, M. J. Cramwinckel, G. R. Dickens, J. Collot, S. J. G. Etienne, A. Bordenave, W. R. Stratford, X. Zhou, H. Li, G. Asatryan
Methodology: R. Sutherland
Software: R. Sutherland
Writing – original draft: R. Sutherland
Writing – review & editing: R. Sutherland, Z. Dos Santos, C. Agnini, L. Alegret, A. R. Lam, T. Westerhold, M. K. Drake, D. T. Harper, E. Dallanave, C. Newsam, M. J. Cramwinckel, G. R. Dickens, J. Collot, S. J. G. Etienne, A. Bordenave, W. R. Stratford, X. Zhou, H. Li, G. Asatryan

Abstract Sediment mass accumulation rate (MAR) is a proxy for paleoceanographic conditions, especially if biological productivity generated most of the sediment. We determine MAR records from pelagic calcareous sediments in Tasman Sea based on analysis of 11 boreholes and >3 million seismic reflection horizon picks. Seismic data from regions of 10,000–30,000 km^2 around each borehole were analyzed using data from International Ocean Discovery Program Expedition 371 and other boreholes. Local MAR was affected by deepwater currents that winnowed, eroded, or deposited seafloor sediment. Therefore, it is necessary to average MARs across regions to test paleoceanographic and productivity models. MARs during the Miocene Climate optimum (18–14 Ma) were slightly lower than Quaternary values but increased on southern Lord Howe Rise at 14–13 Ma, when global climate became colder. Intensification of the Indian and East Asian monsoons at ~8 Ma and ~3.6 Ma approximately corresponds to the start and end, respectively, of the Biogenic Bloom, which had MARs at least double Quaternary values. On northern Lord Howe Rise, we recognize peak MARs at~7 Ma and ~5 Ma. There is no correlation between Neogene MAR and ocean pH or atmospheric CO_2 concentration. Neogene MARs are on average higher than Quaternary values. We posit that future long-term productivity in the southwest Pacific could be higher than Quaternary values, but new computer models that can fit our observations are required to test this hypothesis.

Plain Language Summary Global climate is likely to get warmer, and we want to know what will happen to marine life. We can study ancient warm periods to better predict the future. The ocean is a global carbon sink, because some organisms form shells by combining calcium with carbon dioxide dissolved in seawater. Once dead, their calcium carbonate shells sink to the seabed. Over millions of years, the southwest Pacific accumulated huge deposits. We used geophysical surveying and drilling to measure this history of deposition, which is a proxy for ancient biological productivity (how much marine life existed). A warm period 18–14 million years ago had high atmospheric carbon dioxide (2–4 times preindustrial levels) and slightly lower ocean productivity. In contrast, 8–4 million years ago, atmospheric carbon dioxide was similar to predicted 21st century levels and productivity was much higher: more than double recent values. Rates of calcium carbonate deposition in the past do not correlate with ocean acidity or atmospheric carbon dioxide; but they were mostly higher than today. Hence, long-term biological productivity and carbon sequestration in the southwest Pacific might increase in future, but computer models that fit our observations are needed to test this idea.

1. Introduction

A basic means to establish and understand variations in climate and ocean water properties is through sediment mass accumulation rates (MARs), which are quantified measurements of solid material flux to the seabed (mass

divided by time and area; Equation 1; Brummer & Van Eijden, 1992).

$$\mathrm{MAR} = \rho_{dry} SR \quad (1)$$

where ρ_{dry} is the average dry bulk density and SR is sedimentation rate, which is the observed thickness of a unit divided by the depositional time (difference in age between its base and top). MARs account for changes in porosity during burial, so MARs are a more useful proxy for original input at the seabed. This paper quantifies MARs in Neogene carbonate-rich sediment across northern Zealandia in Tasman Sea, an expansive and relatively shallow (<3,000 m) seafloor area of the southwest Pacific.

Sediment MARs vary across space and time because multiple processes add and remove solid material to and from the seafloor. In general, for pelagic sediment away from continents, MARs primarily relate to the export of biogenic tests formed in surface waters, their dissolution by corrosive undersaturated bottom water, and dilution by siliciclastic and volcanic components (Brummer & Van Eijden, 1992). Changing climate–ocean conditions, such as primary productivity and carbonate saturation horizons, will be manifested in MAR records.

Gravitational settling of biogenic particles in the ocean is of interest to the paleoceanography community, because it is the primary means to shuttle carbon from the shallow ocean to the deep ocean (Berner et al., 1983; Boyd et al., 2019), where it either is stored for centuries in slow-moving deepwater masses or becomes entombed in seabed sediments (at a rate of the MAR multiplied by dry weight % of carbon in sediment). So, how and why has ocean productivity and hence MAR varied during the Neogene in places such as northern Zealandia? Models that can explain past changes over large regions of seafloor may also be able to predict how ocean productivity will change in future.

Deep-sea drilling has revealed an interesting find of global importance in this regard: sediment at numerous open-ocean locations and of late Miocene and early Pliocene age (between 8 and 4 Ma) has much higher MARs for biogenic components (e.g., carbonate, silica, phosphorous, and barium) than previous or subsequent time intervals. This is particularly true for sites in the Pacific and Indian Oceans that lie beneath areas marked by high present-day surface-water productivity (Dickens & Owen, 1999; Drury, Lee, et al., 2018; Farrell et al., 1995; Rea et al., 1991; Van Andel et al., 1975). However, available records suggest that high biogenic sedimentation rates also may have occurred in parts of the Atlantic (Diester-Haass et al., 2004, 2005; Drury, Westerhold, et al., 2018; A. E. Holbourn et al., 2018). The phenomenon of widespread elevated biogenic MARs during the late Miocene and early Pliocene has been coined the "Biogenic Bloom" (Farrell et al., 1995), and its significance lies in realizing that nutrients limit primary productivity in most surface waters and these nutrients have relatively short oceanic residence times. Scores of sites recording elevated biogenic output to the seafloor for several million years implies a greater supply of key nutrient elements to the ocean (e.g., through weathering), a redistribution of key elements within the ocean (e.g., through changes in thermohaline circulation), or both (Dickens & Owen, 1999).

A full appreciation of the Biogenic Bloom needs greater delineation of its global extent. For example, in the eastern equatorial Pacific, sites along the equator show greatly elevated accumulation of biogenic components between 8 and 4 Ma, whereas sites several degrees north do not (Farrell et al., 1995; Lyle, 2003; Van Andel et al., 1975). Of special interest is northern Zealandia, a large submerged continent beneath Tasman Sea in the midlatitudes of the southwest Pacific Ocean (Figure 2). The region has complex oceanography and a seafloor lying above the calcite compensation depth (CCD). Previous work, particularly coming from cores of Deep Sea Drilling Program (DSDP) Leg 90 (Sites 588–593; Figure 2), indicates a Neogene peak in carbonate MARs between 8 and 4 Ma (Grant & Dickens, 2002; Kennett & Von der Borch, 1986). However, MAR records at individual sites may be influenced by sediment transport mechanisms, particularly reworking by bottom currents and sediment gravity flows. So, suggestions for greater biogenic sediment accumulation rate over wide areas of Tasman Sea during the late Miocene and early Pliocene remained tenuous with available data.

Recent results from International Ocean Discovery Program (IODP) Expedition 371 Sites U1506–U1510 (Sutherland et al., 2019) combined with new interpretations of a compilation of many seismic reflection surveys (Sutherland et al., 2012, 2017) provide a strong basis for us to look again at Tasman Sea and to evaluate how MAR values have changed since the Oligocene and identify spatial variability of events such as the late Miocene to Pliocene Biogenic Bloom. We tie seismic reflection mapping to boreholes and resolve regional variability in MAR values through time, and we use spatial averaging to distinguish local depositional effects from regional change. Although we focus on the Neogene, we extend our study back into the Paleogene, because onset of the Antarctic

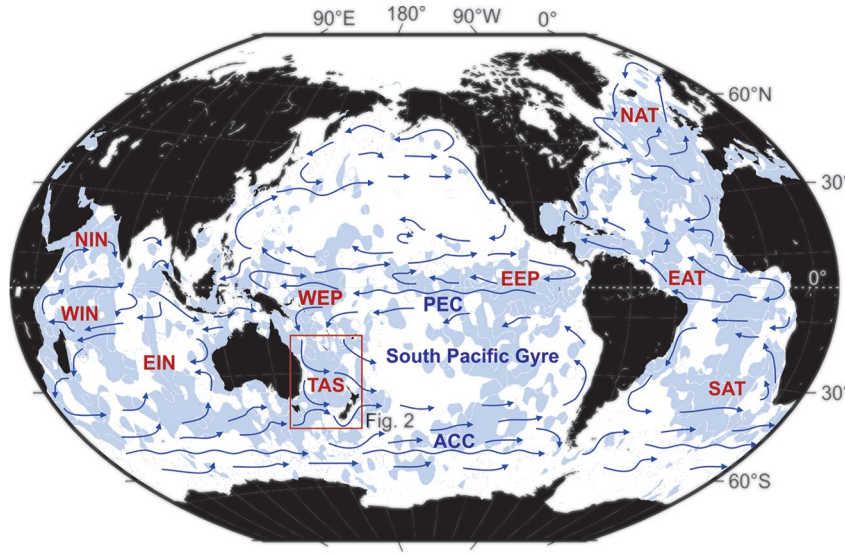

Figure 1. Generalized map of active global ocean currents (blue arrows; after data from www.noaa.gov) and seabed covered in sediment that contains high calcium carbonate content (blue shade; calcareous ooze, mixed calcareous/siliceous ooze, shells and coral fragments, and fine-grained calcareous sediment; Dutkiewicz, Müller, et al., 2015). The South Pacific Gyre has the Pacific Equatorial Current (PEC) to its north and Antarctic Circumpolar Current (ACC) to its south. Region name abbreviations are NIN, northern Indian Ocean; WIN, western Indian Ocean; EIN, eastern Indian Ocean; WEP, western equatorial Pacific; EEP, eastern equatorial Pacific; TAS, Tasman Sea; NAT, northern Atlantic; EAT, equatorial Atlantic; SAT, southern Atlantic. Red box shows the study area (Figure 2).

Circumpolar Current and hence an ocean circulation scenario broadly similar to today was established at around the Eocene–Oligocene boundary (Kennett, 1977). Our greatly enlarged MAR data set provides an observational test for climate models, may be useful to identify targets for future drilling, and our observations of regional MAR variability in the Tasman Sea might be applicable elsewhere.

2. Tasman Sea Setting

Tasman Sea is a prime target for paleoceanographic studies, because it is in a key location between the largest equatorial and subantarctic ocean currents (Figure 1) and has large areas of moderate water depths that are above the CCD (Figure 2). Water depths vary from ~1,000 to 2,000 m on Lord Howe Rise and Norfolk Ridge to ~2,000–3,500 m in New Caledonia Trough (Figure 2). These relatively shallow depths reflect the tectonic origin of underlying crust of northern Zealandia, which is a continental fragment that rifted from eastern Australia in the Cretaceous (Mortimer et al., 2017; Sutherland, 1999). Tasman Abyssal Plain formed between ~83 and 52 Ma, when seafloor spreading opened Tasman Sea (Gaina et al., 1998). Eocene–Oligocene initiation of western Pacific subduction systems caused subsidence of New Caledonia Trough and uplift and deformation (Baur et al., 2014; Sutherland et al., 2010, 2020). The same Eocene event resulted in diffuse deformation (the "tectonic event of the Cenozoic in the Tasman Area," TECTA) and transient shallowing of Lord Howe Rise (Sutherland et al., 2017, 2020). Crust east of Norfolk Ridge was formed by Oligocene to Recent arc and back-arc processes (Herzer et al., 2011; Mortimer et al., 1998; Schellart et al., 2006).

Today, the southward-flowing Eastern Australian Current hugs the eastern margin of Australia as part of a return flow from the westward-flowing Pacific Equatorial Current (Figures 1 and 2). Argo floats show that it penetrates to at least 1,000 m water depths (Chiswell et al., 2015). Westerly winds at midlatitudes drive eastward flow so that a component of this current diverges from Australia into the south Pacific to form a series of easterly flowing ocean fronts and flow filaments (Ridgway & Dunn, 2003). The Tasman Front is a complex field of eddies at the southern edge of the main tropical-derived water mass and currently lies between eastern Australia and northern New Zealand at 31°–36°S latitude (Oke, Pilo, et al., 2019; Oke, Roughan, et al., 2019). By contrast, the Subtropical Front separates the residual Eastern Australian Current from subantarctic water, and it passes just south of New Zealand (H. C. Bostock et al., 2015). South of Australia, the Subantarctic Front, and main flow

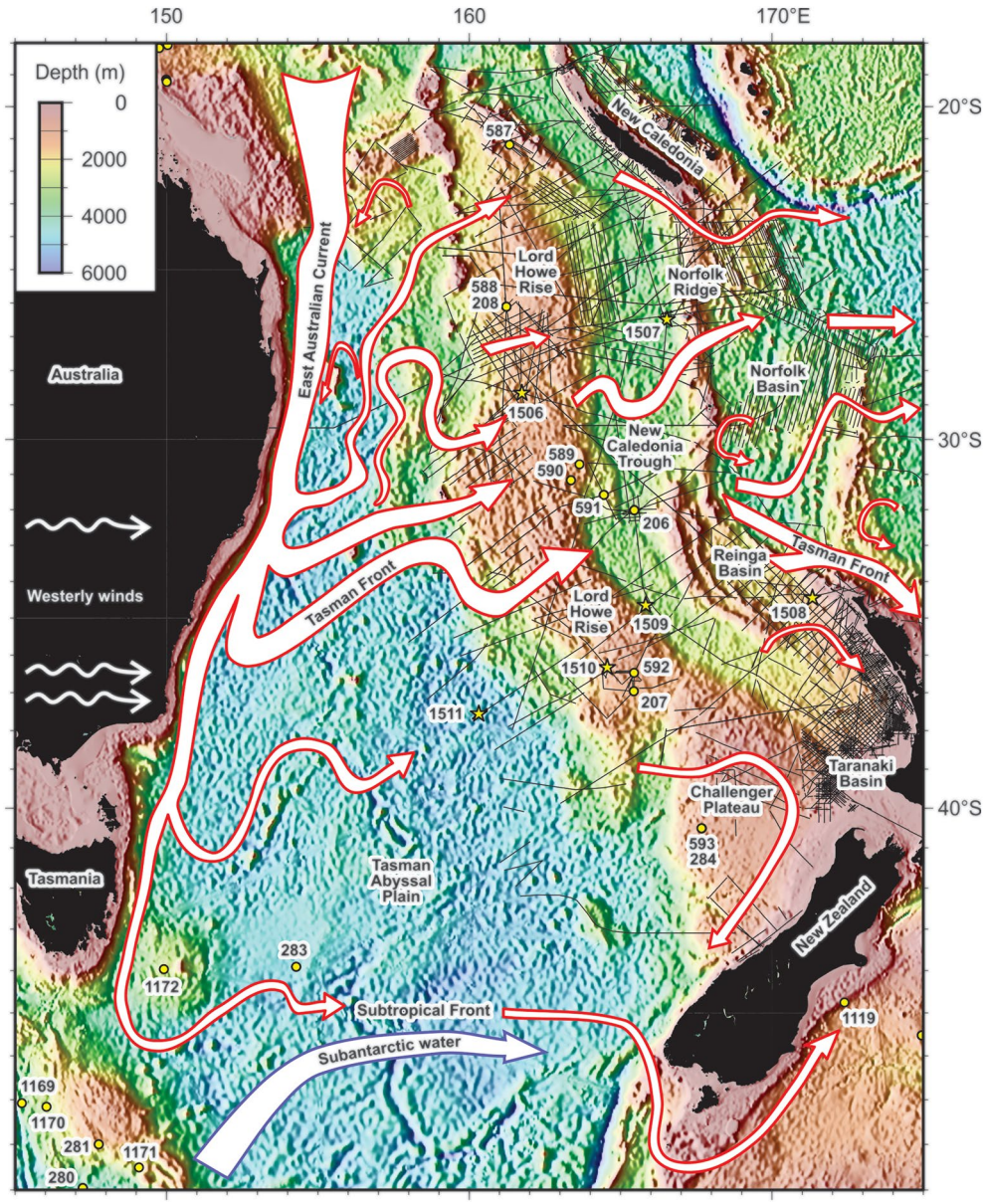

Figure 2. Map of Tasman Sea bathymetry (color shading, ETOPO data set, https://www.ngdc.noaa.gov/mgg/global/) and surface ocean currents (red arrows, white fill) after Ridgway and Dunn (2003). Yellow circles are Deep Sea Drilling Program (DSDP)/International Ocean Discovery Program (IODP) drill sites and yellow stars are IODP Expedition 371 sites. Black lines are locations of seismic reflection data.

of the Antarctic Circumpolar Current (Carter et al., 2008; Rintoul et al., 2001) complete the South Pacific Gyre (Figures 1 and 2).

Deep ocean circulation in Tasman Sea is dominated by Circumpolar Deepwater, because shallow bathymetry of northern Zealandia creates a barrier to Pacific Deepwater (Chiswell et al., 2015). Lower Circumpolar Deepwater forms a northward-flowing boundary current adjacent to Australia (beneath the southward-flowing residual East Australian Current) that diverges eastward beneath the Tasman Front (Chiswell et al., 2015).

The Tasman seabed has been sampled by shallow cores and is carbonate rich in most places except Tasman Abyssal Plain (Figure 3). Noncarbonate terrigenous sediment is found at locations close to land or in and around submarine canyons and troughs that confine gravity flows derived from terrestrial sources. Local highs swept by currents may be encrusted in manganese or/and phosphate and have rich benthic communities of corals and

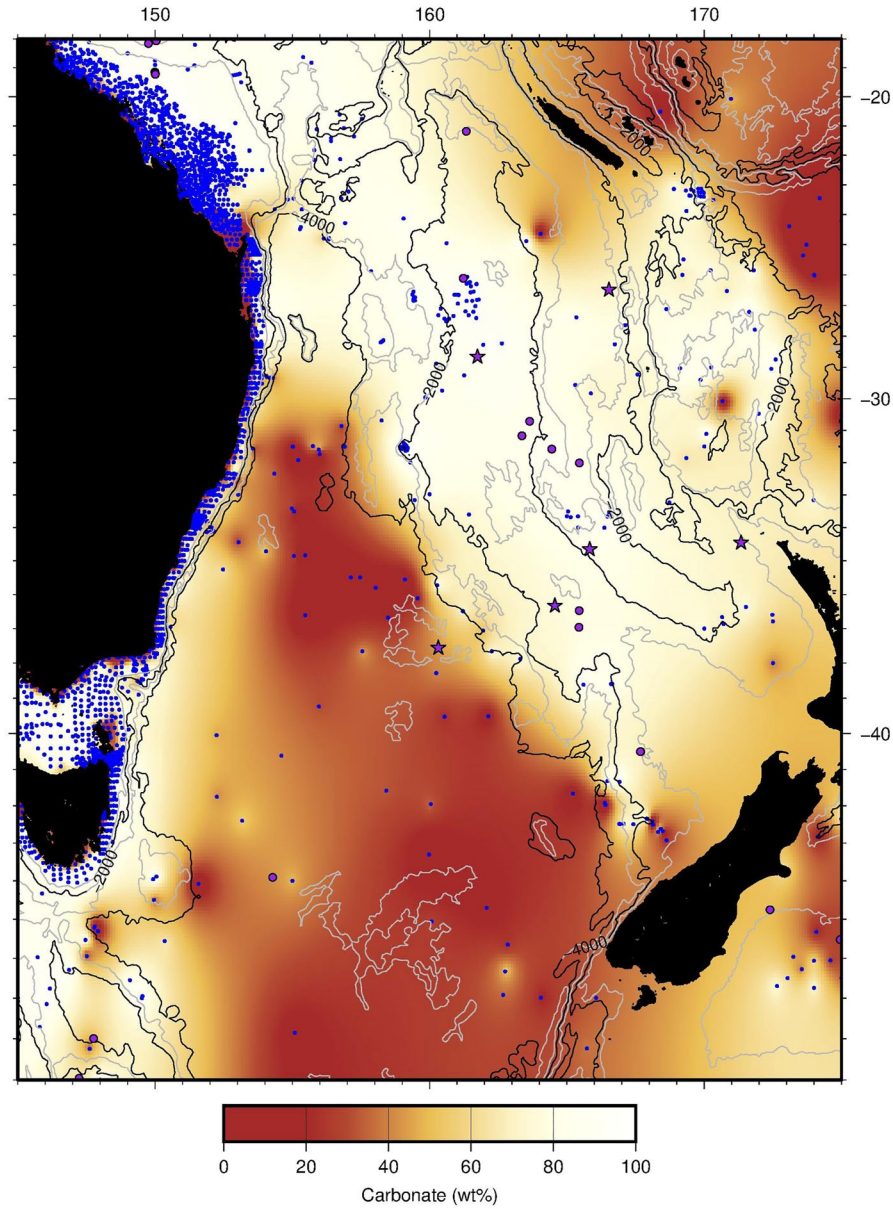

Figure 3. Map of Tasman Sea carbonate content of seabed samples. Data from IODP (http://www.iodp.org/), the Australian Marine Sediments database (MARS, http://dbforms.ga.gov.au/pls/www/npm.mars.search), and from around New Zealand (H. Bostock et al., 2019).

bryozoans (de Forges et al., 2000; Nelson et al., 1982). Tasman Abyssal Plain is clay rich, because it lies well beneath the lysocline, which was at ~3,100–3,600 m depth during the Pleistocene (Martinez, 1994; Figure 4). The CCD varies across the region but is above the abyssal seabed depth (4,500–5,000 m). This has likely been the case for most of the Neogene, based on the thin (<20 m) clay-dominated Neogene sequences sampled at DSDP Site 283 (Kennett et al., 1974) and IODP Site U1511 (Sutherland et al., 2019, 2020; Figure 3).

In this paper, we analyze data from cores of carbonate-rich (generally >80%) Oligocene to Recent sediment recovered from 11 sites that span a wide geographical area with moderate water depths of 1,000–3,600 m (Figures 2–6). We determine multiple bulk sediment MAR history curves for subregions of Tasman Sea, based on analysis of boreholes (Figure 5 and Figures S1–S7 in Supporting Information S1) and seismic reflection data (Figures 7–9 and Figures S8–S14 in Supporting Information S1).

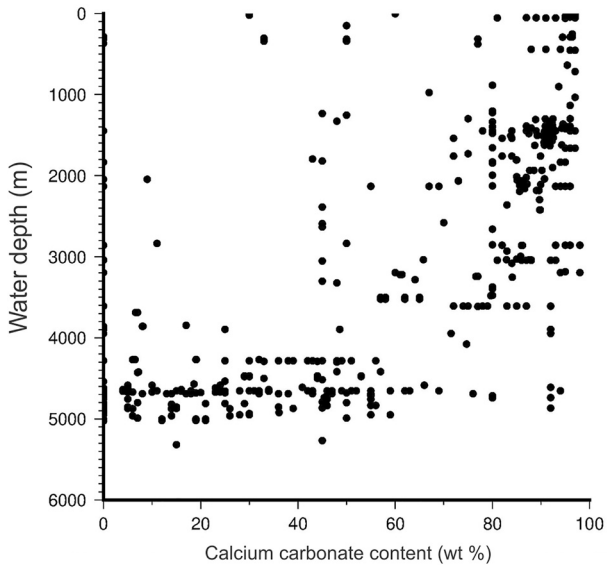

Figure 4. Carbonate content of seabed samples (for locations see Figure 3) plotted as a function of water depth for the Tasman Sea abyssal plain and Lord Howe Rise region (155°–167°E, 25°–43°S). Data sources are the same as Figure 3.

Strata beneath Lord Howe Rise and New Caledonia Trough were first drilled during DSDP Leg 21 at Sites 206, 207, and 208 (Figure 2; Burns et al., 1973). Oligocene to Recent calcium carbonate ooze and chalk overlies siliceous and muddy chalk of Cretaceous to Eocene age, with a regional Eocene–Oligocene unconformity that has been inferred to signify onset of the Antarctic Circumpolar Current (J. Kennett et al., 1972; Kennett, 1977). More sophisticated Advanced Piston Core sampling and multiple coring of the Oligocene to Recent sequence in the same region was carried out during DSDP Leg 90 at Sites 587–593 (Kennett et al., 1986). IODP Expedition 371 sampled new Sites U1506–U1510 (Figure 2; Sutherland et al., 2019). Except for a Pleistocene interval at Site U1509 in Reinga Basin with significant bryozoan fragments, almost all the carbonate consists of calcareous nannofossil and planktonic foraminifera tests (see references above).

3. Methods

3.1. Physical Properties and Ages

Physical property measurements were determined on discrete sediment samples from all sites drilled during IODP Expedition 371. These included wet and dry bulk density, grain density, water content, porosity, and *P* wave velocity (Sutherland et al., 2019). We used meters below seafloor (mbsf) rather than other depth scales (e.g., meters composite depth) which, while constructed to render more complete sections, inflate true depth.

Most sediment in the region has similar grain density (~2,700 kg m^{-3}), so differences in wet and dry bulk density reflect differences in porosity. Downhole trends in physical properties are broadly similar in all the calcareous ooze and chalk intervals that accumulated since the Oligocene. Porosity measurements have higher variability between adjacent samples in the same borehole than they do between boreholes (Figure 6). The exception to this is Site U1508, where there does appear to be significantly higher porosities (Figure 6; possibly due to local overpressure and active migration of hydrocarbons), but it is not clear that U1508 would be representative of the adjacent depocenter, where most of the seismic reflection data that we analyze were collected. For these reasons, we use a single regional compaction model (porosity as a function of depth).

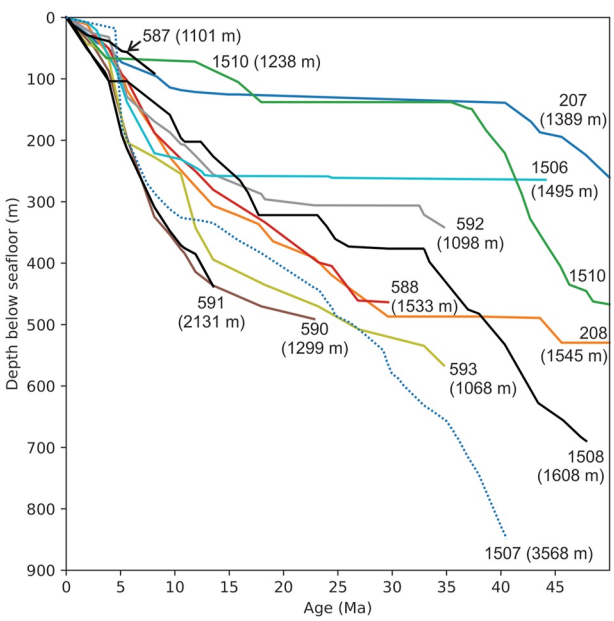

Figure 5. Age versus depth in boreholes considered during this study. For locations see Figure 2, for age models, see Tables S1 and S2 in Supporting Information S1 and Sutherland et al. (2019).

Ages generated for IODP Expedition 371 Neogene sediment sections come primarily from calcareous nannofossils and paleomagnetism, with supporting evidence from foraminifera and radiolaria (Sutherland et al., 2019). Absolute ages of fossil datums were calibrated to the Geological Time Scale 2012 (Gradstein et al., 2012). Microfossil datums for DSDP sites in the region (Burns et al., 1973; Kennett et al., 1986) were reviewed and age models for sedimentation at these sites were updated to reflect currently adopted ages for the biostratigraphic datums (Tables S1 and S2 in Supporting Information S1) and hence they conform with age models used for IODP Expedition 371 (Figure 5).

3.2. MAR Calculation

We calculate total MAR, because it is robust, but note that the concentration of carbonate varies across the region and through time (Figure 6). This correction is discussed later, but not included in our quantitative estimates, because we have insufficient compositional data to build a model of carbonate concentration with space and time. For the late Neogene period of most interest, the carbonate content is consistently ~90% (Figure 6).

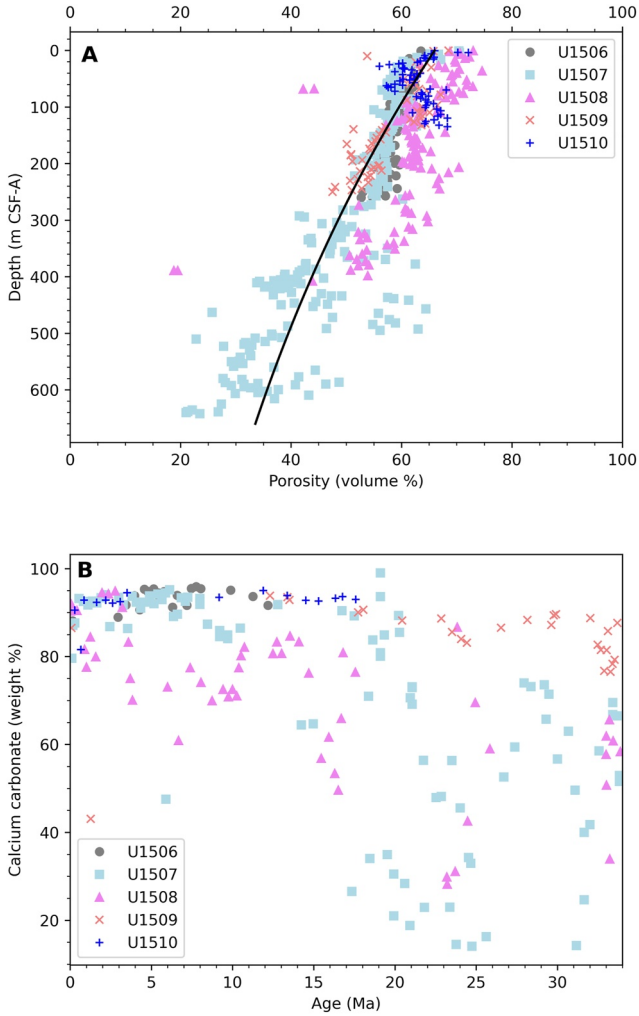

Figure 6. Compilation of relevant data from IODP Expedition 371 (Sutherland et al., 2019). (a) Porosity as a function of depth and (b) calcium carbonate dry weight % as a function of sample age.

We consider the sediment pile as a series of layers and, based on many measurements of samples, assume constant grain density of 2,700 kg m^{-3}. All depths and two-way travel times for seismic reflections are measured downwards and relative to a zero datum at the seabed. The top of layer l is at depth z_l, two-way travel time t_l, and it has age A_l^{top}. The base of layer l is at depth z_{l+1}, two-way travel time t_{l+1}, and has age A_l^{base}. The base of one layer is the top of the next one down, but it may not have the same age if an unconformity exists. We reformulate Equation 1 into Equation 2 to determine MAR at age $A\left(A_l^{top} < A < A_l^{base}\right)$ from layer l.

$$\mathrm{MAR}_A = \frac{\rho_{grain}\int_{z_l}^{z_{l+1}}(1-\phi)dz}{A_l^{base} - A_l^{top}} \tag{2}$$

The porosity ϕ is fit empirically to data as a function of depth (Figure 6 and Equation 3).

$$\phi = \phi_0 e^{-z/L} \tag{3}$$

The best fit model has porosity at the seabed of $\phi_0 = 0.66$ and compaction length $L = 975$ m. We assume a single model for the whole region. Equation 2 can now be solved (see Equation 4) for layers with defined depths and ages for the top and bottom of each layer.

$$\int_{z_l}^{z_{l+1}}(1-\phi)dz = (z_{l+1} - z_l) - \phi_0 L\left(e^{-z_l/L} - e^{-z_{l+1}/L}\right) \tag{4}$$

For borehole data, we take layer boundaries to be the depths of age datums, which gives us maximum temporal resolution. If there are n boreholes in a subregion, we calculate an average MAR for each age from them.

$$\overline{\mathrm{MAR}_A}^{boreholes} = \frac{1}{n}\sum_{i=1}^{i=n}\mathrm{MAR}_A^{borehole\,i} \tag{5}$$

For horizons picked from seismic reflection data, we convert two-way travel time, t, of layer boundaries to depth using an empirical function (Equation 6) determined during IODP Expedition 371 from physical properties measurements, wireline logs, and comparison between seismically interpreted unconformities and borehole results (Sutherland et al., 2019).

$$z = 306.6t^2 + 823.4t \tag{6}$$

The age of each seismic horizon at the borehole was determined using linear interpolation of the borehole age model to the computed depth (Tables S3–S6 in Supporting Information S1). The travel time to the Eocene–Oligocene unconformity can be determined independently from its characteristic reverse polarity (Stratford et al., 2018) and other unconformities provide additional local independent checks on the $z(t)$ relationship, because they can be recognized as breaks in the age model or/and have lithological expression (see Supporting Information S1).

Each common depth point (CDP) on each seismic line that has horizon picks sufficient to define layers that can be tied to at least one borehole can be used to estimate a MAR history. For each region, we calculate a mean (Equation 7) and standard deviation from the m CDPs.

$$\overline{\mathrm{MAR}_A}^{seismic} = \frac{1}{m}\sum_{i=1}^{i=m}\mathrm{MAR}_A^{\mathrm{CDP}\,i} \tag{7}$$

We calculate a combined MAR history (Equation 8) to take advantage of the high temporal resolution of boreholes and high spatial sampling of seismic reflection data.

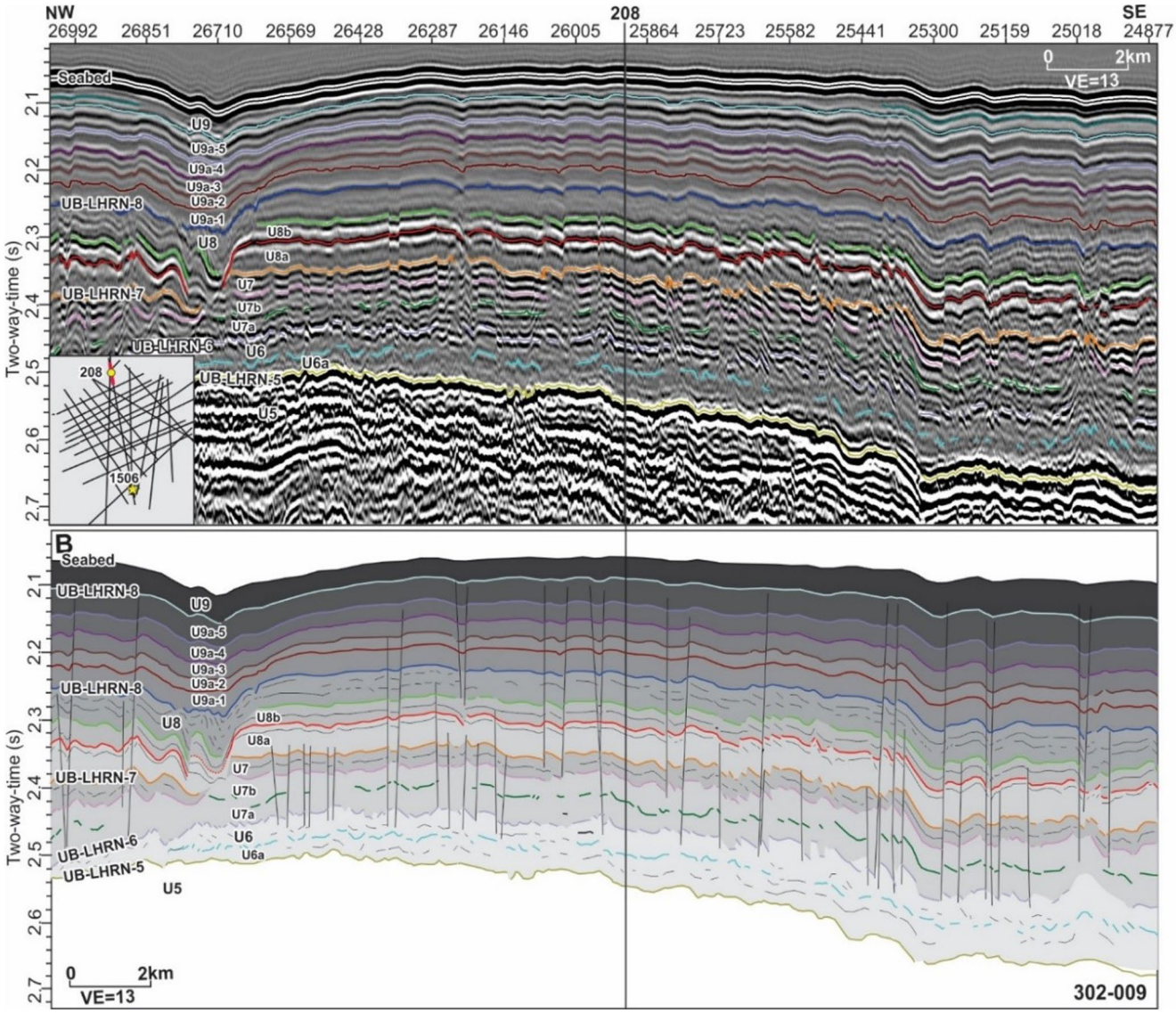

Figure 7. Interpretation of seismic reflection line GA302-009 on northern Lord Howe Rise (LHRN) near Site 208. For ages of reflectors, see Table S3 in Supporting Information S1.

$$\overline{\mathrm{MAR}}_A = \frac{1}{2}\overline{\mathrm{MAR}}_A^{boreholes} + \frac{1}{2}\overline{\mathrm{MAR}}_A^{seismic} \quad (8)$$

The MAR value derived from seismic reflection mapping is given equal weight to that derived from all boreholes in the same analysis, because there are millions of CDPs but only a few boreholes in each region. This approach means that seismic data, which have relatively low temporal resolution but good spatial distribution, influence low-frequency trends in MAR history curves, whereas borehole data provide both high- and low-frequency signals but may contain spatial bias.

3.3. Correlation and Resolution of Seismic Units

Subtle changes in sediment composition over time result in layers with different physical properties and hence seismic impedance. The resulting motifs in seismic reflection images allow regional correlation and mapping of sediment packets away from boreholes over significant distances, and in some cases between boreholes. Two factors interrupt continuity of reflectors and challenge regional mapping: (a) ocean currents and local sediment

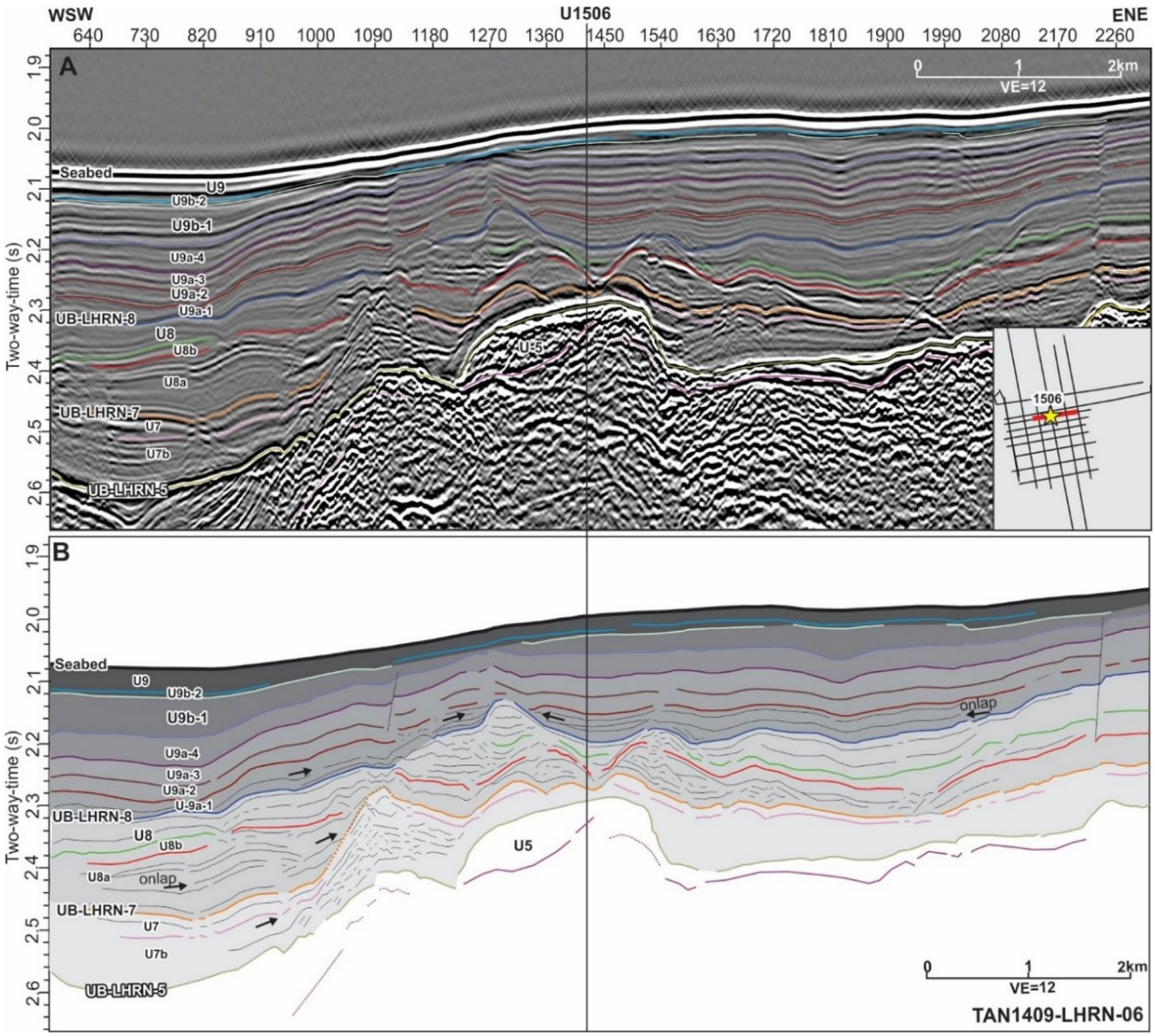

Figure 8. Interpretation of northern Lord Howe Rise high-resolution seismic reflection line TAN1409-LHRN-06 near Site U1506. For ages of reflectors, see Table S3 in Supporting Information S1. Note particularly complex bedforms within U-LHRN-8 (11.9–6.7 Ma) that are interpreted as caused by bottom currents.

gravity flows influence deposition, which means that strata can contain local unconformities or steep bedforms (e.g., channels) and (b) burial causes differential compaction and development of polygonal faults.

Seismic reflection data used in this study were collected using a variety air-gun sources (Sutherland et al., 2012, 2017), but all data reliably image the upper 1 s twt of sediment beneath the seabed, which is all that we require. The frequency content of seismic reflection data limits vertical resolution, with one wavelength typically corresponding to ~30–50 m of depth. Layers that were deposited with high sedimentation rate have relatively small age difference between reflectors, but times of low sedimentation rate have low temporal resolution. Given the ~200–600 m thickness of Oligocene to Recent sediments, we can resolve ~5–15 reflectors, and only some of those occur in distinctive packets that can be mapped regionally. We define as many reflectors as we can at each borehole (e.g., Figures 7–9 and Supporting Information S1) and map them as far as we can reliably. We use nomenclature derived from Bache et al. (2012) for example, U-REIN-9 means seismic unit 9 in Reinga Basin. The corresponding top bounding reflector is named UB-REIN-9. The four-letter code in the middle is an abbreviation that indicates the region.

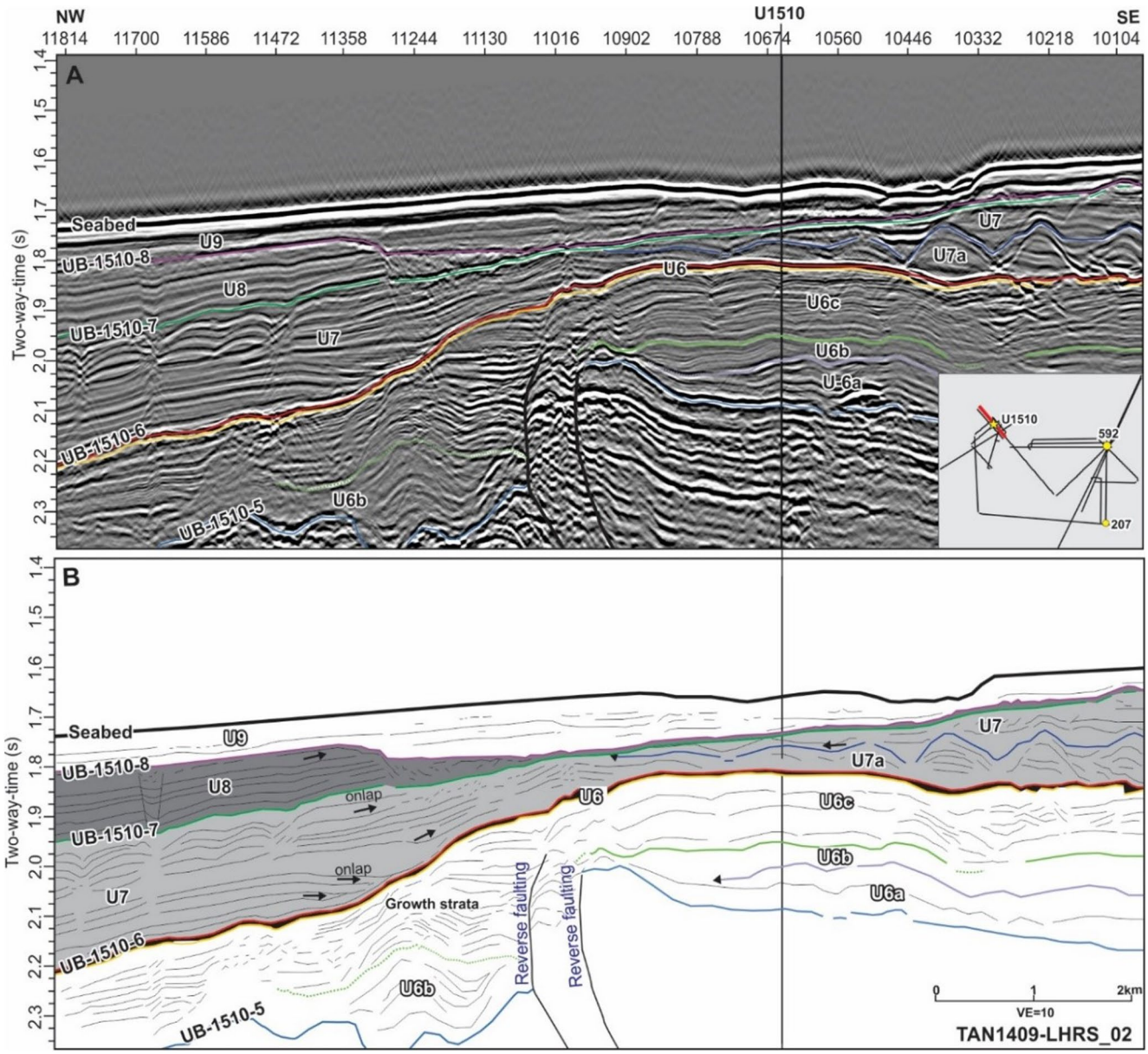

Figure 9. Interpretation of southern Lord Howe Rise high-resolution seismic reflection line TAN1409-LHRS-02 near Site U1510. Note evidence for current scour of U-1510-8 and fill by U-1510-9.

4. Results

4.1. Tasman Sea Subregions

4.1.1. Northern Lord Howe Rise (LHRN)

An excellent high-fold seismic reflection data set (GA302, e.g., Figure 7) images rift basins and overlying Cenozoic sediment in the vicinity of Site 208 (redrilled and triple cored as Site 588) and Site U1506 (Higgins et al., 2015; Sutherland et al., 2019). The Oligocene to Recent sequence is thick and nearly continuous at Site 208 (Figure 7) but has more complex internal geometry near Site U1506 (Figure 8). Most reflectors can be mapped ~295 km between the two borehole sites, and these are given prefix LHRN. A few reflectors are mapped locally near each site and given the site name as a prefix. Figure 11a includes analysis of six borehole sites (U1506, 208, 588, 589, 590, and 591) and seismic mapping near Sites U1506 and 208 (Figure 2).

MAR increased from 5 to 15 kg kyr^{-1} m^{-2} in the late Oligocene (~25 Ma) and then fluctuated in the range 15–20 kg kyr^{-1} m^{-2} from 23 to 13 Ma (Figure 11). MAR rapidly rose to ~30 kg kyr^{-1} m^{-2} at 13 Ma and it is notable that the scatter in MAR values between sites shows high spatial variability during the period 13–8 Ma, suggesting a period of stronger bottom-current activity than the earlier period. During the late Miocene to early Pliocene ~8–3 Ma, there were high accumulation rates that reached peaks of about 50–60 kg kyr^{-1} m^{-2}, with distinct peaks at ~7 Ma and ~5 Ma. There were consistently higher accumulation rates at all sites through late Miocene to early Pliocene time. MAR values during the late Pliocene to Pleistocene fell from 60 to 10 kg kyr^{-1} m^{-2} and seismic reflection mapping reveals significant lateral variability in Quaternary sediment thickness, consistent with strong bottom-current activity.

4.1.2. Southern Lord Howe Rise (LHRS)

Seismic reflection coverage of southern Lord Howe Rise is sparser and more variable in quality than northern Lord Howe Rise. Stratigraphic mapping is also made difficult by the relatively thin units, combined with lateral thickness variations and several volcanic features that interrupt continuity. A region of about 10,000 km^2 was mapped, with age calibration provided by Sites U1510, 207, and 592.

Two unconformities (UB-U1510-8 and UB-U1510-6) were identified at Site U1510 bounding four seismic subunits (Figure 9). Seismic unit U-U1510-6 is Eocene clayey calcareous chalk with bioclasts punctuated by cherty limestone and chert. Folds within U-1510-6 are associated with reverse faults (TECTA) and onlapping growth strata (UB-1510-6a) indicate progressive deformation. An Eocene–Miocene unconformity (reflector UB-LHRS-6, which is equivalent to UB-1510-6 and UB-207-6) was sampled at U1510 and 207, with Oligocene confined to a broad channel feature found near Site 592. Miocene to Pleistocene seismic units U-LHRS-7, U-LHRS-8, and U-LHRS-9 are composed of calcareous ooze. The lower to middle Miocene is mapped regionally as U-LHRS-7, which contains local unconformities interpreted as current scours, and strata onlap older folds and volcanic edifices in the southeast of the mapped region. At Site U1510, there is a hiatus or highly condensed interval that spans 13–4 Ma, which corresponds laterally to a relatively thick unit U-LHRS-8 (Figure 9). Pliocene–Quaternary U-LHRS-9 is generally thin, but can be much thicker in scours, such as found at Site U1510, where beds of foraminiferal ooze have fine sand grain size.

The Oligocene and earliest Miocene is restricted to channel features and topographic lows that we have insufficient data to map adequately, and we have only one borehole (592) for age control. From 18 to 13 Ma, MAR was 8–12 kg kyr^{-1} m^{-2} (Figure 11) and there is evidence for local lateral variability and bottom-current activity. The significant unconformity at Site U1510 reveals a change in current activity and local enhancement of bottom scouring during the interval 13–4 Ma. Seismic unit U-LHRS-8 and Sites 592 and 207 reveal a regional increase in MAR during the late Miocene with peak values of ~30 kg kyr^{-1} m^{-2} at 4–6 Ma. MAR values since 4 Ma have been more variable at 10–20 kg kyr^{-1} m^{-2}, though seismic mapping suggests regional values away from the boreholes, which are located close to the crest of the rise could still be as high as ~30 kg kyr^{-1} m^{-2}.

4.1.3. Northern New Caledonia Trough (NCTN)

Northern New Caledonia Trough was mapped over 15,000 km^2 using high-quality seismic reflection data (Figures S11–S13 in Supporting Information S1). Age and sediment information is derived from Site U1507, which is located on the basin floor adjacent to Norfolk Ridge. The seabed gently slopes toward the axis of the trough, and swath bathymetry images reveal subtle relief associated with basin floor fans that are derived from incised canyons on the lower part of nearby Norfolk Ridge slope (Figure S11 in Supporting Information S1). Seismic reflection interpretation reveals a series of debris flows derived from the flank of Norfolk Ridge, and sediment cores from Site U1507 contain abundant evidence for sediment gravity flows derived from the ridge. Therefore, MAR values derived from around Site U1507 broadly reflect MAR from the flank of Norfolk Ridge but are higher than local pelagic sedimentation rates, because we have mapped a local depocenter that accumulates sediment from a broader region through concentration by sediment gravity flows to the basin floor.

Eocene chalk and limestone correspond to seismic unit U-NCTN-5 (43–37 Ma). Eocene to early Miocene seismic units U-NCTN-6 (37–24 Ma) and U-NCTN-7 (24–20 Ma) are clayey chalk and volcanic turbidites derived from a large submerged volcano near the crest of Norfolk Ridge (Figure S11 in Supporting Information S1; Sutherland et al., 2019), where dredging yielded a volcanic age of 26 Ma (Mortimer et al., 2018). Seismic units U-NCTN-7, U-NCTN-8, and U-NCTN-9 comprise clayey calcareous ooze and chalk with many reworked fossils (Sutherland

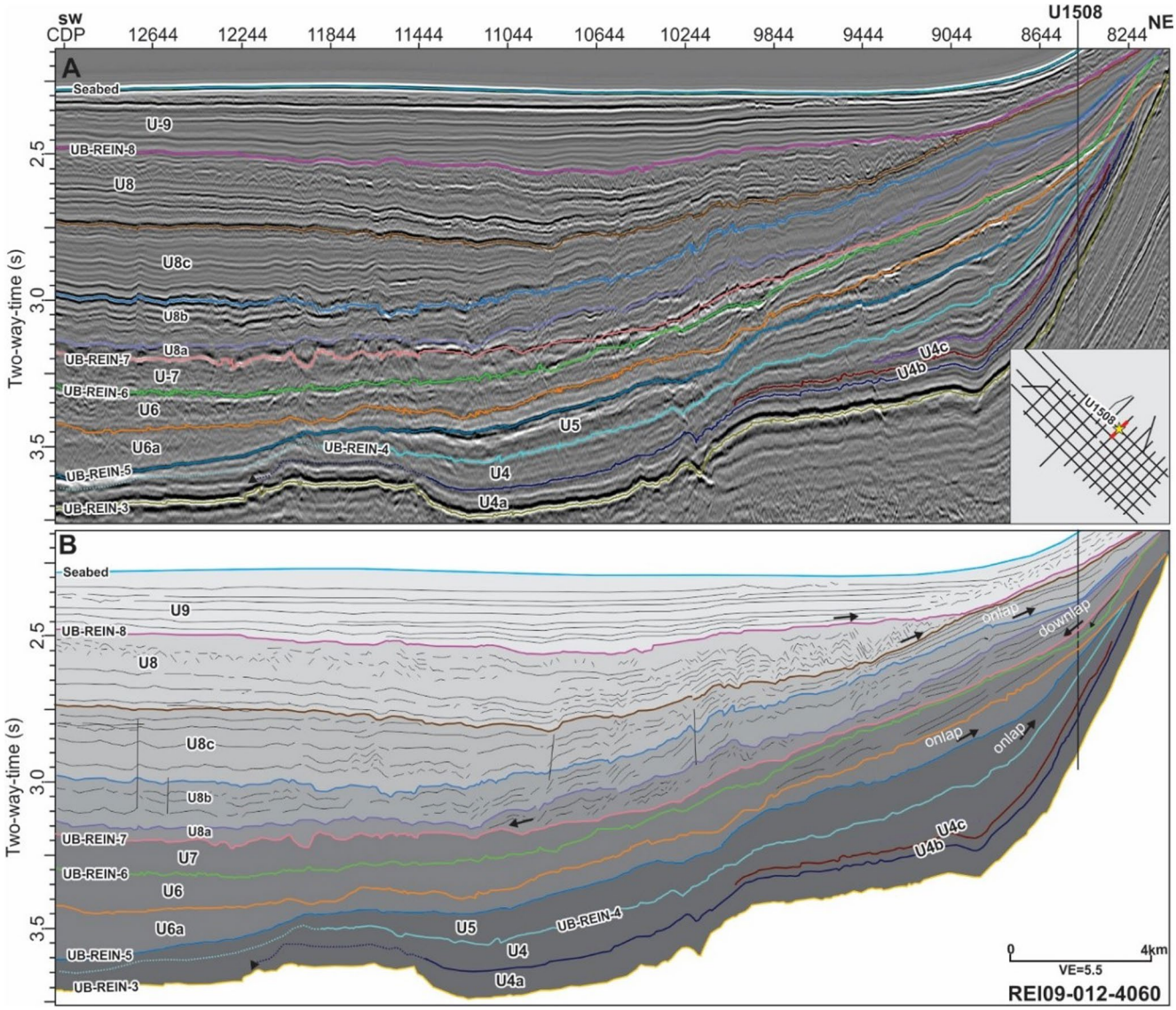

Figure 10. Interpretation of Reinga Basin high-resolution seismic reflection line REI09-012 near Site U1508. Note expansion of U-REIN-8 in the basin axis as a hiatus is developed on the basin flank near Site U1508.

et al., 2019). There is erosion by gravity flows at the base of U-NCTN-8. U-NCTN-7 and U-NCTN-8 are affected by polygonal faults.

Seismic subunits U-NCTN-9b and U-NCTN-9c are onlapped by a major infilling unit with horizontal laterally continuous moderate-amplitude reflectors with intercalated bodies of transparent to chaotic facies interpreted as large-scale mass transport deposits. Consequently, we reinterpret the two first-occurrence biostratigraphic datums in this sequence as reworked from older sediment at the basin flank and obtain a revised age model with uniform sedimentation rate since 5 Ma (red line in Figure S6 in Supporting Information S1), that is, there is no age control on Pliocene–Quaternary stratigraphy. The presence of *Amaurolithus primus* beneath 17.8 m and abundant evidence for gravity flows is consistent with rapid deposition during the Biogenic Bloom and subsequent reworking of that sediment, that is, high pelagic input during the Biogenic Bloom causing slope instability and gravity flows, with probably lower (unresolved) Quaternary rates of pelagic sediment input.

MAR dropped from 50 to 60 kg kyr^{-1} m^{-2} in the Eocene–Oligocene to 6–12 kg kyr^{-1} m^{-2} at 13–11 Ma (Figure 10) but note that calcium carbonate concentration of Oligocene and early Miocene sediments was in many cases <50%

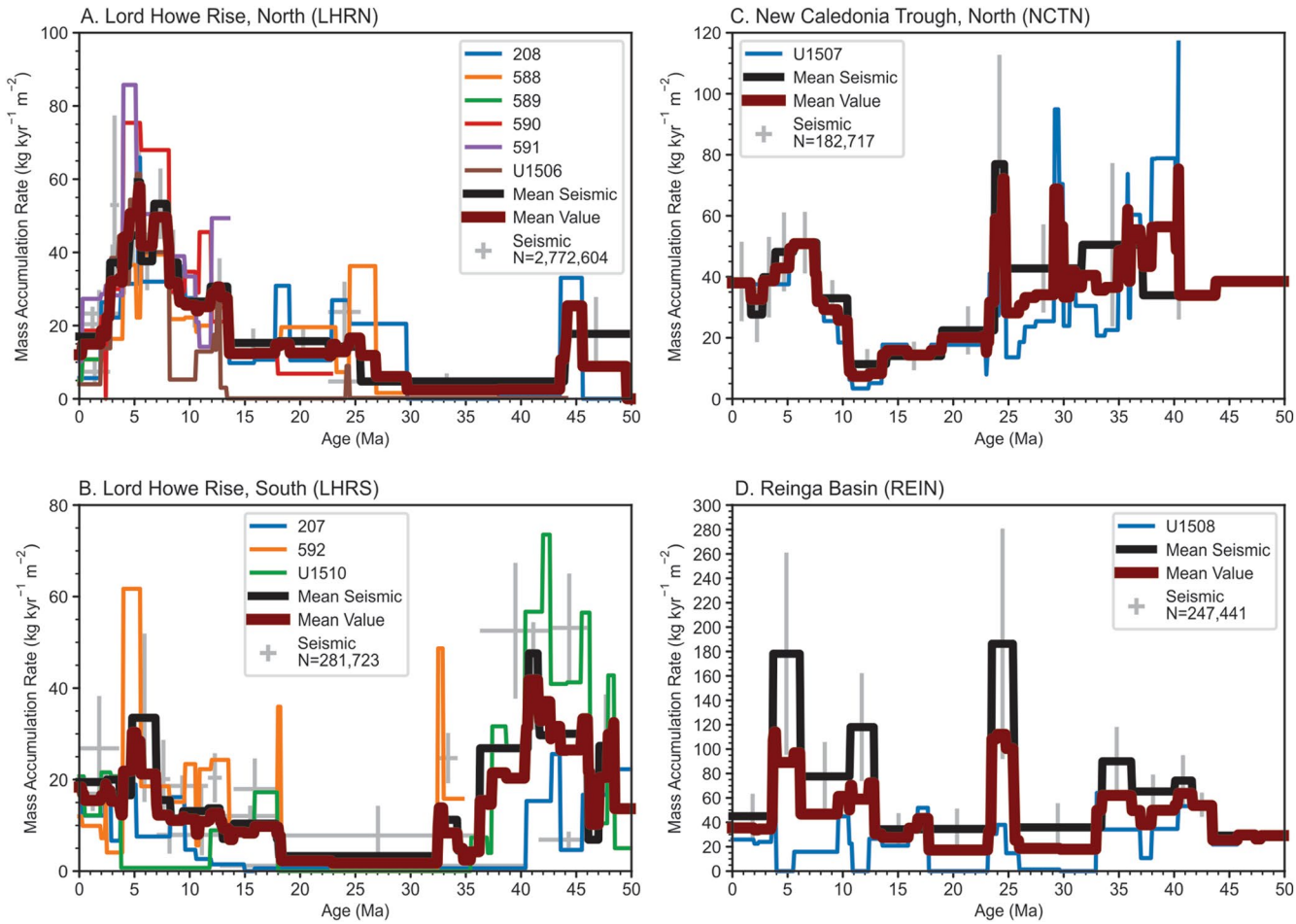

Figure 11. Mass accumulation rate (MAR) values for regional averages of seismic reflection units (vertical error bar is one standard deviation of spatial variability). Solid red line is weighted mean of all boreholes and seismic interpretation, with equal weight given to amalgamated boreholes and regional seismic interpretation.

due to volcaniclastic input. MAR increased from 11 Ma to ~50 kg kyr^{-1} m^{-2} at 8–5 Ma (Figure 11). There is relatively poor age control on strata younger than 5 Ma, but the average MAR since 5 Ma was 30–40 kg kyr^{-1} m^{-2}.

4.1.4. Reinga Basin (REIN)

A high-quality seismic reflection data set exists for Reinga Basin and we mapped a region of 30,000 km^2 near Site U1508. We follow previous seismic unit nomenclature (Bache et al., 2012; Orr et al., 2020). U-REIN-4 and U-REIN-5 (48–34 Ma) are composed of folded, faulted, and onlapping reflectors that record progressive TECTA deformation (Figure 9). U-REIN-6 and U-REIN-7 (34–13 Ma) have fanning reflectors that onlap and downlap, and volcanic and clastic input is evident in channelized slope deposits. U-REIN-8 and U-REIN-9 (13–0 Ma) are drape strata with an architecture related to variable bottom-current strength and regional productivity.

Site U1508 is at the base of South Maria Ridge, which is the northern extension of the New Zealand land mass and is where the southern edge of the Tasman Front is constricted and concentrated by the bathymetric barrier of New Zealand. Consequently, this part of Reinga Basin experiences strong bottom currents and has a relatively condensed sequence. Quaternary sediment at Site U1508 (1,609 m water depth) is foraminiferal sand with coarse bioclasts (mainly bryozoan; Sutherland et al., 2019). In the axis of the basin at 1,500–2,500 m water depth, Quaternary dune bedforms reach >100 m wavelength and >5 km axial length (Sutherland et al., 2019).

Unconformities developed in the past on current-swept ridges while enhanced sedimentation filled axial basins. MAR was high (>100 kg kyr^{-1} m^{-2}) during the Oligocene and early Miocene but substantial dilution of carbonate by terrigenous and volcanic material is evident at Site U1508 (Figure 6; Sutherland et al., 2019). MAR values were relatively low and constant at 20–40 kg kyr^{-1} m^{-2} from 18 to 13 Ma, but this is a similar or higher value to

that found at the same time on southern Lord Howe Rise. A hiatus during 13–11 Ma at U1508 corresponds to U-REIN-8 in the basin axis, where a high MAR of 80–160 kg kyr^{-1} m^{-2} is determined. U-REIN-9 (11–0 Ma) is characterized by contourites and other types of drift sediment and is subdivided by a hiatus (6–4 Ma) at U1508. Seismic reflection interpretation yields high MAR values in the basin axis during deposition of this unit: 50–100 kg kyr^{-1} m^{-2} at 11–6 Ma; 100–260 kg kyr^{-1} m^{-2} at 6–4 Ma; and 30–60 kg kyr^{-1} m^{-2} at 4–0 Ma.

5. Discussion

5.1. Overall Tasman Sea

We restrict discussion of MARs in Tasman Sea to regions with moderate water depths (<3,500 m and mostly <2,500 m) and avoid Sites 283 and U1511 (Figure 2), because they have low MARs and clay-rich sediment indicating they were below the CCD for much of the Neogene (Burns et al., 1973; Sutherland et al., 2019). Bulk sediment MARs within Oligocene and Neogene strata of northern Zealandia in eastern Tasman Sea vary over space and time (Figure 11). Incorporating interpretations of seismic reflection data enhances results from drill sites, because local variability associated with deposition (dunes, contourites, drifts, and sediment gravity flows) and erosion or mass-wasting is averaged. Boreholes show that most sediment is carbonate (Figure 6), so MARs are robust features that mostly reflect sedimentation rates of biogenic clasts. Exceptions to this are the Oligocene and early Miocene of Reinga Basin (REIN) and northern New Caledonia Trough (NCTN). We break our discussion into four general time intervals.

Interpretation of Oligocene and early Miocene (34–18 Ma) MAR values is complicated by a series of tectonic effects that involved deformation, uplift, and volcanism. An influx of noncarbonate sediment components explains relatively high MAR values at eastern sites: northern New Caledonia Trough and Reinga Basin (Orr et al., 2020; Sutherland et al., 2019). After considering this dilution, the average biogenic component of MAR in the Oligocene and early Miocene was low (<20 kg kyr^{-1} m^{-2}; Figure S15 in Supporting Information S1). Southern Lord Howe Rise has very little late Oligocene to early Miocene sediment and a hiatus marks this time interval at all borehole sites.

From 18 to 14 Ma, bulk sediment MARs were fairly uniform across northern Zealandia at 10–20 kg kyr^{-1} m^{-2} (Figure 12). Seismic mapping suggests Reinga Basin may have had slightly higher MAR of 20–40 kg kyr^{-1} m^{-2}, but this may partly express production over a greater area than mapped (includes submarine ridges) that supplied sediment that was concentrated and deposited in the basin depocenter. Bedforms related to bottom currents are evident, but we do not observe local thickness variability to the same extent as in younger strata.

An onset of higher MAR and enhanced current activity began between 14 and 11 Ma. This interpretation is most obvious from records in Reinga Basin, where an unconformity is developed on South Maria Ridge and basin axis MAR values jump to >100 kg kyr^{-1} m^{-2} at ~13 Ma (Figure 11). Northern Lord Howe Rise also experienced an approximate doubling of MAR values at 14–13 Ma. Interestingly, a significant increase in MAR happened in northern New Caledonia Trough later at ~11 Ma and the age model at Site U1507 provides good control over the interval 14–8 Ma. No clear change in MARs occurred during the middle Miocene on southern Lord Howe Rise (Figure 12), but this may partly reflect difficulty in dating sediment of this age, because a hiatus exists at Site U1510 from 13 to 4 Ma. The hiatus onset probably indicates stronger current action after 13 Ma, as also inferred for sediment on the flanks of Reinga Basin. Reinga Basin has very high MARs in the basin axis during hiatus development at Site U1508 (Figure 12), and a high MAR value is found at 14–11 Ma at Site U1509, which lies just east (downstream of current flow; Figure 2) of southern Lord Howe Rise (Sutherland et al., 2019). Strong currents swept ridges and concentrated pelagic sedimentation into adjacent troughs.

The expected effects of the hypothesized Biogenic Bloom are evident in all four regions: MAR values reveal a broad Neogene maximum at ~9–4 Ma. The maximum MAR value in each region during this interval was about double the value at 10 Ma. Peak MARs occurred at ~5 Ma, more than one peak may be resolvable with additional higher-resolution work (especially evident for northern Lord Howe Rise). The development of stratal terminations, local unconformities, and high spatial variability in layer thicknesses attests to strong bottom-current activity during the Biogenic Bloom, especially during the peak of the event.

After 4 Ma, MAR values dropped back to moderate levels (Figure 12), but there is abundant seismic-stratigraphic evidence for strong bottom-current activity (drifts, dunes, contourites, etc., e.g., see Figure S14 in Supporting Information S1).

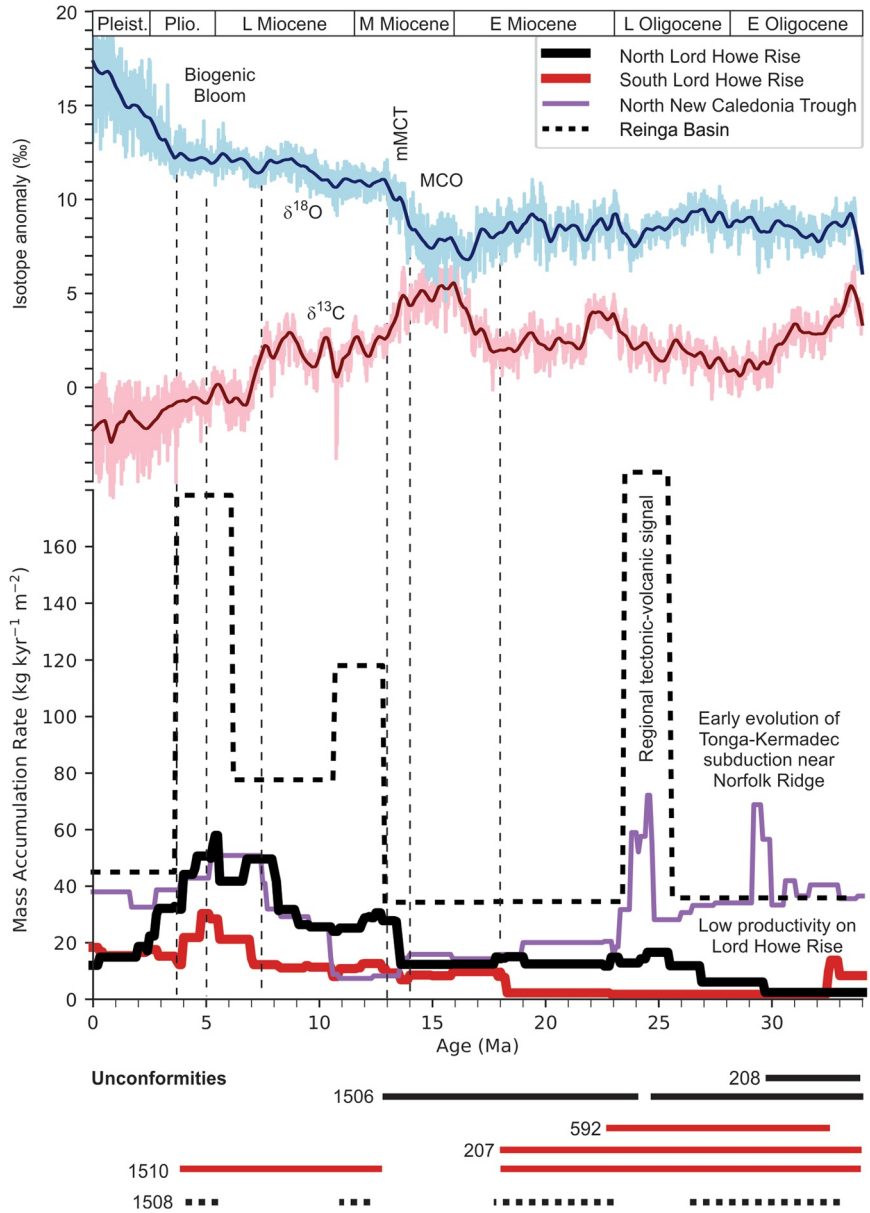

Figure 12. Synthesis of regional MAR values compared with global stacks of oxygen and carbon isotopes (Westerhold et al., 2020). The regional seismic-derived estimate for Reinga Basin is used rather than the mean value, because the single borehole at Site U1508 is not at all representative of regional values and would bias the result. However, note that Reinga Basin values are high, because productivity from surrounding regions where a hiatus is present accumulated in the basin axis, where we mapped.

5.2. Relationships to Neogene Climate Change

During the Oligocene and early Miocene, bulk sediment MARs in the Tasman Sea were affected by regional tectonic evolution of the Australia–Pacific plate boundary. This included volcanic and sedimentary input near Norfolk Ridge, and vertical tectonic movements that changed bathymetric depths (Orr et al., 2020; Sutherland et al., 2020). Miocene MARs before the Miocene Climate Optimum (MCO, 17–14 Ma) and middle Miocene Climate Transition (mMCT, 14–13 Ma; B. P. Flower & Kennett, 1994) on Lord Howe Rise were uniform and low (Figure 12). Seismic-stratigraphic interpretation suggests that moderate bottom currents were active during the early Miocene at bathyal depths on Lord Howe Rise.

Fossils from New Zealand indicate a warm ocean during the early Miocene. Reef-building corals similar to those in the Great Barrier Reef today (sea surface temperature [SST], 19°C–28°C) were well established and diverse around northern North Island (Hornibrook, 1992). Oxygen and carbon isotopes of bathyal benthic foraminifera from northern Lord Howe Rise (Site 588) were used by B. P. Flower and Kennett (1994) to argue for a warm (tropical) saline source of deep and intermediate water. A tropical shallow Pacific Ocean circulation system similar to the present day is implied, though our data show that it produced lower biological productivity and had lower-strength bottom currents than those of the Pleistocene.

The MCO is identified in benthic foraminiferal $\delta^{18}O$ records as a ~1‰ negative shift (Vincent & Berger, 1985; Westerhold et al., 2020; Zachos et al., 2001). The MCO was a time when global average temperatures increased in response to elevated atmospheric CO_2 concentrations, which range from glacial levels to almost double the Holocene preindustrial value (e.g., Cerling, 1991; B. P. Flower & Kennett, 1994; Kucharavy & De Guio, 2011; Pagani et al., 1999; Pearson & Palmer, 2000; Royer et al., 2001), with warming possibly linked to eruption of the Columbia River Basalts (Kasbohm & Schoene, 2018). During the latter phase of the MCO (~16–14 Ma), upper ocean conditions inferred from planktonic foraminiferal calcite in the northern (ODP Site 588) and southern (ODP Site 1171) Tasman Sea indicate progressive warming and/or salinity changes in the mixed layer and thermocline, with $\delta^{18}O$ and $\delta^{13}C$ values generally beginning to decline around 15.5 Ma (B. Flower & Kennett, 1993; Shevenell et al., 2004).

Despite a stable bottom water source and changing surface ocean conditions, productivity throughout Tasman Sea remained low during the MCO, as inferred from low MAR values across this event (Figure 12). Low MAR values through this interval may also be explained by some shoaling of the lysocline during warmest periods of the MCO, as evidenced from sites in the eastern equatorial Pacific and subtropical southwest Pacific (A. Holbourn et al., 2007, 2014; Kochhann et al., 2016), but the water depths of our sites are significantly less than most predictions for CCD variation during the Neogene (Sosdian et al., 2018).

During the mMCT, MARs on northern Lord Howe Rise nearly doubled from MCO levels (Figure 12). Interestingly, MARs on southern Lord Howe Rise remain at MCO levels throughout the mMCT, indicating some latitudinal control on processes that affected MAR on this bathymetric high (e.g., intensification of a proto Tasman Front during the mMCT).

Proxy data from high latitudes (~55°S) south of Tasmania suggest an SST drop in the Southern Ocean (south of our study region; Figure 2) of 6°C–7°C during the mMCT as the East Antarctic ice sheet expanded and stabilized, and the Antarctic Circumpolar Current and Southern Hemisphere Polar Vortex strengthened (Groeneveld et al., 2017; A. Holbourn et al., 2013, 2014; Shevenell et al., 2004). South of Tasmania at Site U1171 (Figure 2), there is evidence for a minor (~2°C) and transient SST rebound (warming, 13.8–13.7 Ma) after the mMCT main phase of ice sheet growth (Shevenell et al., 2008), which can be explained using coupled atmosphere–ocean models as resulting from a complex interplay between winds, ocean circulation, and sea ice (Knorr & Lohmann, 2014). These models predict warming of northeastern Australia, strengthening of westerly winds, and strengthening of the shallow subtropical circulation in the Tasman Sea during the mMCT. This is consistent with evidence for the onset of aridification in eastern Australia (Locker & Martini, 1989; Martin, 2006).

Records across the mMCT from equatorial to mid latitude regions indicate increased productivity in both the marine (A. Holbourn et al., 2014; Vincent & Berger, 1985) and terrestrial realms (Diester-Haass et al., 2009). Notably, increased productivity through upwelled thermocline waters began during the mMCT in the eastern equatorial Pacific and was concurrent with increased carbonate preservation (A. Holbourn et al., 2014; Lyle & Baldauf, 2015). Results of MAR from northern Lord Howe Rise match carbonate MAR results from sites in the western equatorial Pacific (WEP; Si & Rosenthal, 2019).

Oceanographic models for the mMCT predict more vigorous ocean circulation in Tasman Sea (Knorr & Lohmann, 2014). Unconformities and high spatial variability in MAR developed in southern Tasman Sea (southern Lord Howe Rise; Reinga Basin flanks) during and after the mMCT, consistent with strong bottom currents, but average regional MARs on southern rises did not significantly increase, as far as our data allow us to quantify it (Figure 12). Nearby southern New Caledonia Trough records cannot easily be used, because they contain high terrigenous input, as do younger records from Challenger Plateau (near Site 593). Our observations of elevated MAR values at subtropical sites close to the Tasman Front are broadly consistent with previous studies (e.g., Si & Rosenthal, 2019).

After the mMCT, evidence from IODP sites west of Australia suggests a progressive northward migration of the zone of westerly winds from 12 to 8 Ma (Groeneveld et al., 2017). The increase in MAR we observe in Tasman Sea after the mMCT may be related to one or all of the main factors involved in nutrient supply: increased ocean current strength; increased supply of nutrient-rich cold Antarctic-derived deep and intermediate water; and increased quantities of wind-blown dust from Australia (aridification, northward migration of westerlies, and increased wind strength).

The beginning and end of the Biogenic Bloom approximately correspond with significant intensifications of the Indian and East Asian monsoons at ~8 Ma and then again at 3.6 Ma (A. E. Holbourn et al., 2018; Zhisheng et al., 2001). Aridification of eastern Asia and eastern Australia intensified at 8 Ma (Zheng et al., 2004; Zhisheng et al., 2001), with late Miocene burning of Australian *Eucalyptus* forest becoming common (Martin, 2006). The East Asian monsoon resulted in loess deposits onshore and upwelling offshore, increased delivery of wind-blown dust to the ocean, and higher productivity in the western Pacific (Zheng et al., 2004; Zhisheng et al., 2001). The SST difference between the western and eastern equatorial Pacific was steady at 2°C–3°C or slightly dropped during the period 12–8 Ma and then increased during and after the Biogenic Bloom (Zhang et al., 2014). At higher latitudes, strong cooling may have been slightly later at ~7–5 Ma (Herbert et al., 2016). Stronger currents (upwelling at divergence zones), increased wind-blown nutrient supply, combined with expansion of nutrient-rich Antarctic deep and intermediate waters may all explain higher inferred productivity in the Tasman Sea during the Biogenic Bloom.

Grant and Dickens (2002) analyzed elemental ratios and carbon isotopes of Biogenic Bloom (8–4 Ma) sediment at Site 590 (Figures 2 and 12). They found abundant evidence for elevated primary productivity, but elemental ratios Ca/Ti, Ba/Ti, and Al/Ti peak at 6.5 Ma (likely reflecting peak terrigenous input), whereas MAR (total average productivity) peaks at 5 Ma. Bulk sediment carbon isotope shifts (Figure 12) can be explained by combined effects of changing whole ocean composition, isotopic depth stratification, and changing types of primary productivity with different depth habitats. Hence, Grant and Dickens (2002) inferred asynchronous changes in nutrient supply and hydrography during the Biogenic Bloom.

Our results confirm that there is a clear MAR peak in the Tasman Sea at ~5 Ma, but northern Lord Howe Rise and possibly northern New Caledonia Trough have an earlier peak at 8–6 Ma or had relatively uniform MAR through the interval 8–5 Ma. The eastern equatorial Pacific at Site U1338 reveals that between 8.0–6.5 and 5.2–4.4 Ma, low east-west $\delta^{18}O$ and SST gradients and generally warm conditions prevailed; and diverging fine-fraction-to-coarse fraction foraminiferal $\delta^{13}C$ gradients suggest increased upwelling between 7.1–6.0 and 5.8–4.6 Ma (Drury, Lee, et al., 2018; Lyle & Baldauf, 2015). Our work suggests that there exists some fine structure within the Biogenic Bloom in the Tasman Sea that might be correlated to records elsewhere.

De Vleeschouwer et al. (2020) note a reorganization of the climate–carbon cycle system at ~6 Ma, during the Biogenic Bloom, with the change in influence of Arctic cooling included as a causal factor: continental carbon reservoirs expanded during global cool spells before 6 Ma, but the opposite was true after 6 Ma. Drury, Westerhold, et al. (2018) found distinct, asymmetric cycles in benthic stable isotope data from sediments of the North Atlantic that indicate high-latitude climate processes related to ice sheet dynamics pace climate variability in the interval 7.7–6.7 Ma. Increasing influence of obliquity driven climate variability is reported from higher northern latitudes (ODP 982; Drury, Westerhold, et al., 2018) as well as the equatorial Pacific (U1337, U1338; Drury, Westerhold, et al., 2017; A. E. Holbourn et al., 2018) already occurring at 7.7 Ma and further strengthening at 6.4 Ma. Thus, the processes leading to the increase in MAR seen in the Tasman Sea region seem to be linked to global scale shifts in Earth's climate response to orbital pacing related to polar ice volume evolution (Westerhold et al., 2020). It is clear that global changes during the Biogenic Bloom had a long-term impact on global and southwest Pacific Ocean climate processes. The exact timing and mechanisms of forcing and feedbacks in the Tasman Sea region need to be resolved at much finer details than presented here. Laborious studies that can resolve astronomical cycles and produce very precise age model are needed to test causality arguments.

Changes in east Asia at 3.6 Ma resulted in even more arid conditions than those of the late Miocene and higher rates of loess accumulation onshore and delivery to the western Pacific (Zheng et al., 2004; Zhisheng et al., 2001). The Quaternary climate of eastern Australia is even drier now than it was in the late Miocene (Martin, 2006), and zonal SST differences in the equatorial Pacific have increased from 8°C to 10°C since 4 Ma (Zhang et al., 2014). There has clearly been growth of the Antarctic ice sheets and expansion of Antarctic

deep water after 3.6 Ma (Naish et al., 2009). These Pacific-wide changes all had the same sense as those at ~8 Ma, but MAR values in the Tasman Sea are lower since 3.6 Ma. We observe seismic-stratigraphic evidence for intensification of bottom-current action in the Tasman Sea after 3.6 Ma (e.g., Figure 9 and Figures S8 and S14 in Supporting Information S1), but average productivity has been approximately half that of the Biogenic Bloom, and northern Lord Howe Rise (our best determined values) has reduced to just 30%. Our work confirms previous results from the western Pacific (e.g., Si & Rosenthal, 2019).

Si and Rosenthal (2019) postulate that cooler climates and reduced atmospheric carbon dioxide led to lower rates of weathering, reduced alkalinity input to the ocean, and less marine calcification (particularly coccolithophores). They argue that low carbon availability in the photic ocean limited growth sizes and rates of coccoliths and that this was a significant factor that led to lower MAR values. However, we see no obvious correlation in our data between MAR values and atmospheric CO_2 or ocean pH in the past (Figure 13; Rae et al., 2021). Mechanisms and drivers that controlled marine biological productivity changes in the past remain obscure. Previous studies (e.g., Grant & Dickens, 2002) suggest complex relationships between Tasman Sea productivity and causal factors

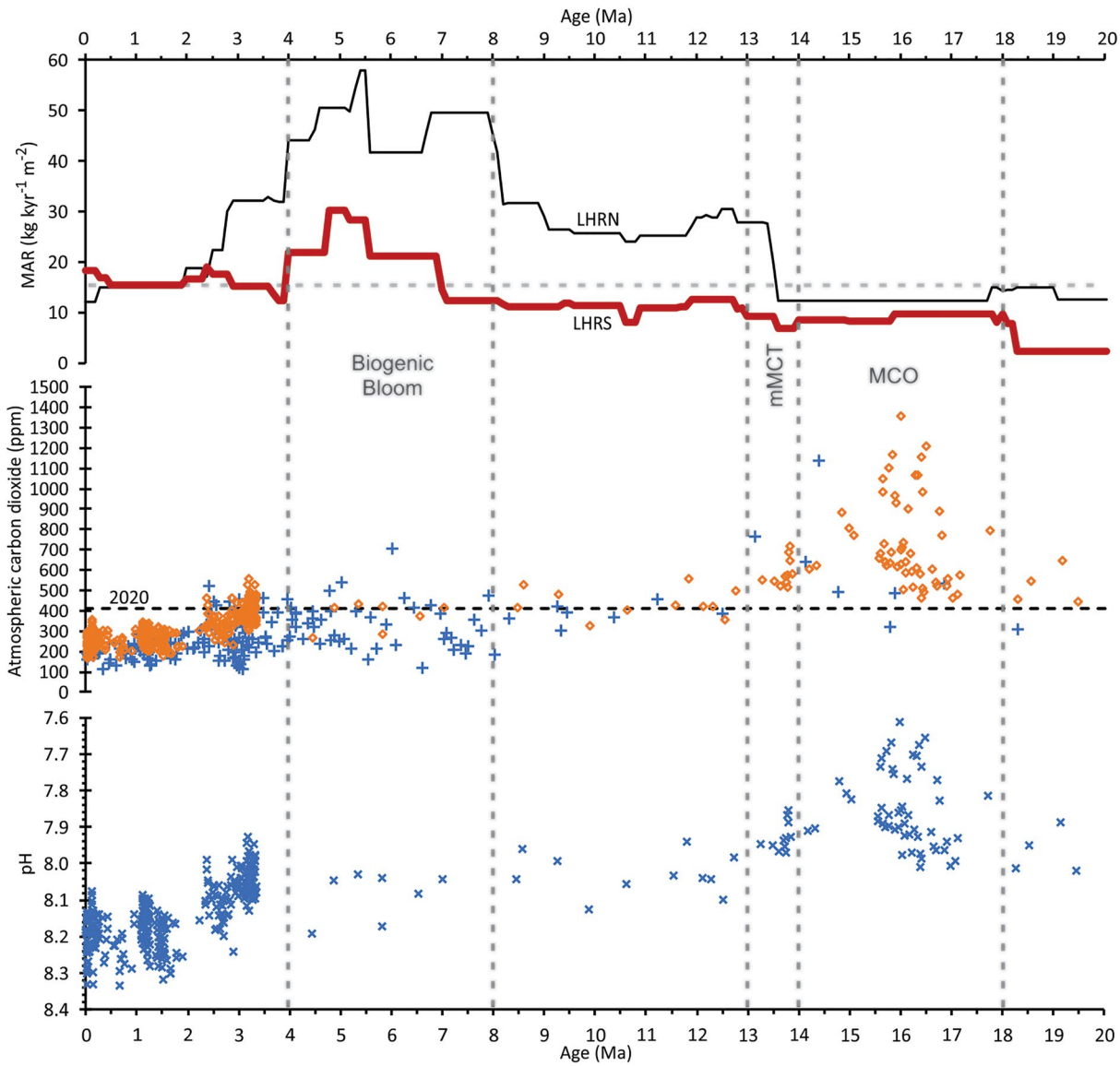

Figure 13. MAR on northern (LHRN) and southern (LHRS) Lord Howe Rise compared with estimates of atmospheric CO_2 and ocean pH in the past. Atmospheric CO_2 estimates are based on either boron isotopes (blue crosses) or alkenones (orange diamonds), and ocean pH was calculated from $\delta^{11}B$ of borate (Rae et al., 2021).

of nutrient type (wind-blown dust, river suspended or dissolved loads, and upwelling deep water) and delivery (wind, precipitation, and ocean current patterns), and it could be that global climate cooling and lowering of atmospheric carbon dioxide has also played some bigger role (Si & Rosenthal, 2019).

6. Conclusions and Future Climate Change

We present an analysis of Tasman Sea MARs based on a revised biostratigraphic and compaction analysis of 11 boreholes and >3 million seismic reflection horizon picks tied to those boreholes. We depth converted seismic reflection interpretations and accounted for compaction using physical properties data from IODP Expedition 371. We analyzed a region of 10,000–30,000 km^2 around each borehole, but the total size of northern Zealandia is ~3 × 10^6 km^2.

Our study shows that regional variability in MAR is significant, due to the action of deepwater currents that have winnowed, created hiatuses, or eroded sediment at the seabed (1,000–3,000 m depth) in some places and deposited bedforms (drifts, contourites, dunes, fans, etc.) in others. Therefore, it is necessary to average MARs over larger areas to obtain estimates that can be used to infer past ocean productivity. Individual boreholes may provide misleading results and can be strongly affected by their specific location. Regional mapping in the context of bathymetry and paleoceanographic models provides the information needed to target future work at meaningful sites and allows more insightful interpretation of existing borehole sites. For example, Site U1508 has hiatuses at times of highest regional productivity, because strong currents that delivered nutrients to the region also scoured the seabed at that specific location. MAR observations provide useful tests for climate models, but it is essential to integrate seismic-stratigraphic interpretation with borehole studies in regions where bottom currents or gravity flows have modified pelagic depositional processes. For Tasman Sea, this is most of the region.

We see significant increases in MAR as global climate became colder and Antarctic ice sheets grew at ~14–13 Ma, during the mMCT; and then again as the east Asian monsoons developed at ~8 Ma at the start of the Biogenic Bloom. MAR peaked in the Tasman Sea during the Biogenic Bloom at 5 Ma, but an earlier peak at 8–6 Ma is also evident in northern Tasman Sea, where Grant and Dickens (2002) show terrigenous input peaked at 6.5 Ma at Site 590 (though remained a small value). Although large-scale global cooling and aridification trends were the same at 8 and 4 Ma, climate responses to orbital (and other shorter timescale mechanisms of) forcing have changed. Cooler climates since 4 Ma coincided with lower MAR values in the southwest Pacific, and average MAR values since 3 Ma have dropped to just 30%–50% of their value at 5 Ma.

Biogenic particles settling in the ocean and exporting carbon toward the seabed play a key role in long-term modulation of atmospheric carbon dioxide (Boyd et al., 2019) and may play a key role in the eventual natural (or engineered) remediation of our climate crisis. It seems certain that our future world will be warmer and have carbon dioxide concentration significantly elevated above preindustrial levels: we are heading back toward conditions similar to those of the Pliocene and Miocene (Figure 13). There is a widespread concern that ocean acidification might lead to a profound change or even collapse in the ocean ecosystem over coming centuries, with a resulting reduction in calcium carbonate deposition (Dutkiewicz, Morris, et al., 2015). However, because we do not fully understand the drivers of MAR change, it remains unclear to us whether the southwest Pacific will eventually have lower rates of marine productivity and calcium carbonate deposition (natural carbon sequestration), as was present during the MCO, or if they will be higher, as they were during the Biogenic Bloom (Figure 13). There is no correlation between long-term (Myr scale) carbonate MAR and atmospheric CO_2 (Figure 14; or past ocean pH), and MAR values from the late Quaternary are among the lowest of all Neogene values. We posit that, although the rate of atmospheric CO_2 change this century may be much greater than changes in the past, it remains a viable possibility that global warming could lead to future long-term increases in biological productivity and carbon export in the southwest Pacific. We do not claim to understand the mechanisms involved but suggest that further work is urgently required to develop models that can explain the geological past, so that we can have more confidence in predicting how biological productivity will change during coming decades and centuries.

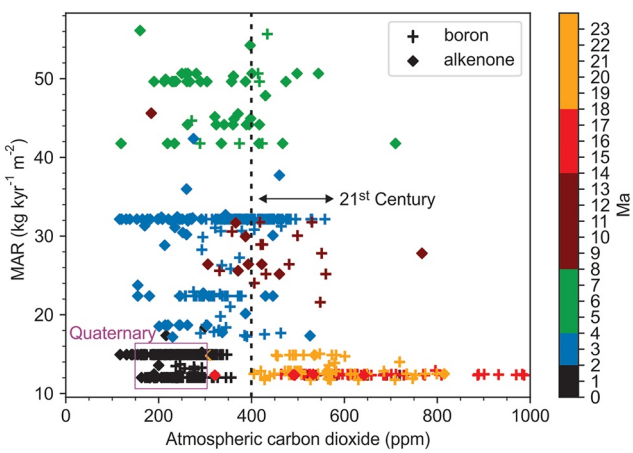

Figure 14. MAR on northern Lord Howe Rise (LHRN) since 23 Ma plotted against estimates of atmospheric CO_2 based on boron isotopes (blue crosses) and alkenones (orange diamonds; Rae et al., 2021).

Data Availability Statement

Digital files of seismic horizon picks, age models, and code (that could be reused for analysis of other regions) are available at https://github.com/RupertSutherland/sedBasin (https://doi.org/10.5281/zenodo.5502246). Seismic reflection data were compiled, described, and made available by Sutherland et al. (2012) and are most easily obtained from GNS Science (https://data.gns.cri.nz/pbe) or New Zealand Petroleum & Minerals (https://data.nzpam.govt.nz). TECTA 2015 data (NCTN region) are available from https://doi.org/10.17600/15001300 and by typing in "TECTA" in the search bar at IFREMER: https://donnees-campagnes.flotteoceanographique.fr/search (embargo until 2022). TAN1409 data can be obtained from https://data.gns.cri.nz/pbe. ETOPO data set: https://www.ngdc.noaa.gov/mgg/global/. IODP data: https://www.iodp.org/resources/access-data-and-samples. Australian Marine Sediments database, MARS: http://dbforms.ga.gov.au/pls/www/npm.mars.search.

Acknowledgments
We thank International Ocean Discovery Program (IODP), especially crew and technical staff involved in Expedition 371; scientists involved in proposal writing or work onboard; the Associate Editor, Yige Zhang; reviewer Mitch Lyle; and two anonymous reviewers. *Funding*: NSF and many other national funding organizations that support IODP; ED is supported by DFG Project number 408178503; TW by DFG Project number 446583469; and LA by project PID2019-105537RB-I00 (Spanish Ministry of Science and Innovation and FEDER funds). Seisware software was used for seismic interpretation. GNS Science helped build the seismic reflection data set. Open access publishing facilitated by Victoria University of Wellington, as part of the Wiley - Victoria University of Wellington agreement via the Council of Australian University Librarians.

References

Bache, F., Stagpoole, V., & Sutherland, R. (2012). *Seismic stratigraphy of the Reinga Basin, NW New Zealand: Tectonic and petroleum implications*. Paper presented at the New Understanding of the Petroleum Systems of Continental Margins of the World.

Baur, J., Sutherland, R., & Stern, T. (2014). Anomalous passive subsidence of deep-water sedimentary basins: A prearc basin example, southern New Caledonia Trough and Taranaki Basin, New Zealand. *Basin Research*, *26*(2), 242–268.

Berner, R., Lasaga, A., & Garrels, R. (1983). The carbonate–silicate geochemical cycle and its effect on atmospheric carbon dioxide over the past 100 million years. *American Journal of Science*, *283*(641), 641–683.

Bostock, H., Jenkins, C., Mackay, K., Carter, L., Nodder, S., Orpin, A., et al. (2019). Distribution of surficial sediments in the ocean around New Zealand/Aotearoa. Part A: Continental slope and deep ocean. *New Zealand Journal of Geology and Geophysics*, *62*(1), 1–23.

Bostock, H. C., Hayward, B. W., Neil, H. L., Sabaa, A. T., & Scott, G. H. (2015). Changes in the position of the Subtropical Front south of New Zealand since the last glacial period. *Paleoceanography*, *30*, 824–844. https://doi.org/10.1002/2014PA002652

Boyd, P. W., Claustre, H., Levy, M., Siegel, D. A., & Weber, T. (2019). Multi-faceted particle pumps drive carbon sequestration in the ocean. *Nature*, *568*(7752), 327–335.

Brummer, G., & Van Eijden, A. (1992). "Blue-ocean" paleoproductivity estimates from pelagic carbonate mass accumulation rates. *Marine Micropaleontology*, *19*(1–2), 99–117.

Burns, R. E., Andrews, J. E., van der Lingen, G. J., Churkin, M., Galehouse, J. S., Packham, G., et al. (1973). *Initial reports of the Deep Sea Drilling Project Leg 21* (Vol. 21). U.S. Government Printing Office.

Carter, L., McCave, I., & Williams, M. J. (2008). Circulation and water masses of the Southern Ocean: A review. *Developments in Earth and Environmental Sciences*, *8*, 85–114.

Cerling, T. E. (1991). Carbon dioxide in the atmosphere: Evidence from Cenozoic and Mesozoic paleosols. *American Journal of Science*, *291*(4), 377–400.

Chiswell, S. M., Bostock, H. C., Sutton, P. J., & Williams, M. J. (2015). Physical oceanography of the deep seas around New Zealand: A review. *New Zealand Journal of Marine & Freshwater Research*, *49*(2), 286–317.

de Forges, B. R., Koslow, J. A., & Poore, G. (2000). Diversity and endemism of the benthic seamount fauna in the southwest Pacific. *Nature*, *405*(6789), 944–947.

De Vleeschouwer, D., Drury, A. J., Vahlenkamp, M., Rochholz, F., Liebrand, D., & Pälike, H. (2020). High-latitude biomes and rock weathering mediate climate–carbon cycle feedbacks on eccentricity timescales. *Nature Communications*, *11*(1), 1–10.

Dickens, G. R., & Owen, R. M. (1999). The latest Miocene–early Pliocene Biogenic Bloom: A revised Indian ocean perspective. *Marine Geology*, *161*(1), 75–91.

Diester-Haass, L., Billups, K., & Emeis, K. C. (2005). In search of the late Miocene–early Pliocene "Biogenic Bloom" in the Atlantic Ocean (Ocean Drilling Program Sites 982, 925, and 1088). *Paleoceanography*, *20*, PA4001. https://doi.org/10.1029/2005PA001139

Diester-Haass, L., Billups, K., Gröcke, D. R., François, L., Lefebvre, V., & Emeis, K. C. (2009). Mid-Miocene paleoproductivity in the Atlantic Ocean and implications for the global carbon cycle. *Paleoceanography*, *24*, PA1209. https://doi.org/10.1029/2008PA001605

Diester-Haass, L., Meyers, P., & Bickert, T. (2004). Carbonate crash and Biogenic Bloom in the late Miocene: Evidence from ODP Sites 1085, 1086, and 1087 in the Cape Basin, southeast Atlantic Ocean. *Paleoceanography*, *19*, PA1007. https://doi.org/10.1029/2003PA000933

Drury, A., Lee, G., Gray, W., Lyle, M., Westerhold, T., Shevenell, A. E., et al. (2018). Deciphering the state of the late Miocene to early Pliocene equatorial Pacific. *Paleoceanography and Paleoclimatology*, *33*, 246–263. https://doi.org/10.1002/2017PA003245

Drury, A. J., Westerhold, T., Frederichs, T., Tian, J., Wilkens, R., Channell, J. E., et al. (2017). Late Miocene climate and time scale reconciliation: Accurate orbital calibration from a deep-sea perspective. *Earth and Planetary Science Letters*, *475*, 254–266.

Drury, A. J., Westerhold, T., Hodell, D., & Röhl, U. (2018). Reinforcing the North Atlantic backbone: Revision and extension of the composite splice at ODP Site 982. *Climate of the Past*, *14*(3), 321–338.

Dutkiewicz, A., Müller, R. D., O'Callaghan, S., & Jónasson, H. (2015). Census of seafloor sediments in the world's ocean. *Geology*, *43*(9), 795–798.

Dutkiewicz, S., Morris, J. J., Follows, M. J., Scott, J., Levitan, O., Dyhrman, S. T., et al. (2015). Impact of ocean acidification on the structure of future phytoplankton communities. *Nature Climate Change*, *5*(11), 1002–1006.

Farrell, J. W., Raffi, I., Janecek, T. R., Murray, D. W., Levitan, M., Dadey, K. A., et al. (1995). Late Neogene sedimentation patterns in the eastern equatorial Pacific Ocean. In *Proceedings of the Ocean Drilling Program, Scientific Results*. Ocean Drilling Program.

Flower, B., & Kennett, J. (1993). Middle Miocene ocean–climate transition: High-resolution oxygen and carbon isotopic records from Deep Sea Drilling Project Site 588A, southwest Pacific. *Paleoceanography*, *8*(6), 811–843.

Flower, B. P., & Kennett, J. P. (1994). The middle Miocene climatic transition: East Antarctic ice sheet development, deep ocean circulation and global carbon cycling. *Palaeogeography, Palaeoclimatology, Palaeoecology*, *108*(3–4), 537–555.

Gaina, C., Mueller, D. R., Royer, J.-Y., Stock, J., Hardebeck, J. L., & Symonds, P. (1998). The tectonic history of the Tasman Sea: A puzzle with 13 pieces. *Journal of Geophysical Research*, *103*(6), 12413–12433.

Gradstein, F. M., Ogg, J. G., Schmitz, M. D., & Ogg, G. M. (2012). *The geologic time scale 2012*. Elsevier.

Grant, K. M., & Dickens, G. R. (2002). Coupled productivity and carbon isotope records in the southwest Pacific Ocean during the late Miocene–early Pliocene Biogenic Bloom. *Palaeogeography, Palaeoclimatology, Palaeoecology*, *187*(1), 61–82.
Groeneveld, J., Henderiks, J., Renema, W., McHugh, C. M., De Vleeschouwer, D., Christensen, B. A., et al. (2017). Australian shelf sediments reveal shifts in Miocene Southern Hemisphere westerlies. *Science Advances*, *3*(5), e1602567.
Herbert, T. D., Lawrence, K. T., Tzanova, A., Peterson, L. C., Caballero-Gill, R., & Kelly, C. S. (2016). Late Miocene global cooling and the rise of modern ecosystems. *Nature Geoscience*, *9*(11), 843–847.
Herzer, R., Barker, D., Roest, W., & Mortimer, N. (2011). Oligocene–Miocene spreading history of the northern South Fiji Basin and implications for the evolution of the New Zealand plate boundary. *Geochemistry, Geophysics, Geosystems*, *12*, Q02004. https://doi.org/10.1029/2010GC003291
Higgins, K., Hashimoto, T., Rollet, N., Colwell, J., Hackney, R., & Milligan, P. (2015). Structural analysis of extended Australian continental crust: Capel and Faust Basins, Lord Howe Rise. *Geological Society, London, Special Publications*, *413*(1), 9–33.
Holbourn, A., Kuhnt, W., Clemens, S., Prell, W., & Andersen, N. (2013). Middle to late Miocene stepwise climate cooling: Evidence from a high-resolution deep water isotope curve spanning 8 million years. *Paleoceanography*, *28*, 688–699. https://doi.org/10.1002/2013PA002538
Holbourn, A., Kuhnt, W., Lyle, M., Schneider, L., Romero, O., & Andersen, N. (2014). Middle Miocene climate cooling linked to intensification of eastern equatorial Pacific upwelling. *Geology*, *42*(1), 19–22.
Holbourn, A., Kuhnt, W., Schulz, M., Flores, J.-A., & Andersen, N. (2007). Orbitally-paced climate evolution during the middle Miocene "Monterey" carbon-isotope excursion. *Earth and Planetary Science Letters*, *261*(3–4), 534–550.
Holbourn, A. E., Kuhnt, W., Clemens, S. C., Kochhann, K. G., Jöhnck, J., Lübbers, J., et al. (2018). Late Miocene climate cooling and intensification of southeast Asian winter monsoon. *Nature Communications*, *9*(1), 1–13.
Hornibrook, N. de B. (1992). New Zealand Cenozoic marine paleoclimates: A review based on the distribution of some shallow water and terrestrial biota. In *Pacific Neogene: Environment, evolution, and events* (pp. 83–106). University of Tokyo Press.
Kasbohm, J., & Schoene, B. (2018). Rapid eruption of the Columbia River flood basalt and correlation with the mid-Miocene Climate Optimum. *Science Advances*, *4*(9), eaat8223.
Kennett, J. P., Burns, R., Andrews, J., Churkin, M., Davies, T., Dumitrica, P., et al. (1972). Australian–Antarctic continental drift, palaeocirculation changes and Oligocene deep-sea erosion. *Nature Physical Science*, *239*, 51–55.
Kennett, J. P. (1977). Cenozoic evolution of Antarctic glaciation, circum-Antarctic ocean, and their impact on global paleoceanography. *Journal of Geophysical Research*, *82*(27), 3843–3860.
Kennett, J. P., Houtz, R. E., Andrews, P. B., Edwards, A. R., Gostin, V. A., Hajos, M., et al. (1974). Site 283. In *Initial Reports of the Deep Sea Drilling Project* (Vol. 29, pp. 365–402). U.S. Government Printing Office.
Kennett, J. P., & Von der Borch, C. C. (1986). Southwest Pacific Cenozoic paleoceanography. *Initial Reports of the Deep Sea Drilling Project*, *90*, 1493–1517. Retrieved from http://deepseadrilling.org/90/volume/dsdp90pt2_48.pdf
Kennett, J. P., von der Borch, C. C., Baker, P. A., Barton, C. E., Boersma, A., Caulet, J. P., et al. (1986). *Initial reports of the Deep Sea Drilling Project covering Leg 90 of the cruises of the Drilling Vessel Glomar Challenger; Noumea, New Caledonia, to Wellington, New Zealand, December 1982–January 1983* (Vol. 90). U.S. Government Printing Office.
Knorr, G., & Lohmann, G. (2014). Climate warming during Antarctic ice sheet expansion at the Middle Miocene transition. *Nature Geoscience*, *7*(5), 376–381.
Kochhann, K. G., Holbourn, A., Kuhnt, W., Channell, J. E., Lyle, M., Shackford, J. K., et al. (2016). Eccentricity pacing of eastern equatorial Pacific carbonate dissolution cycles during the Miocene Climatic Optimum. *Paleoceanography*, *31*, 1176–1192. https://doi.org/10.1002/2016PA002988
Kucharavy, D., & De Guio, R. (2011). Logistic substitution model and technological forecasting. *Procedia Engineering*, *9*, 402–416.
Locker, S., & Martini, E. (1989). Phytoliths at DSDP site 591 in the southwest Pacific and the aridification of Australia. *Geologische Rundschau*, *78*(3), 1165–1172.
Lyle, M. (2003). Neogene carbonate burial in the Pacific Ocean. *Paleoceanography*, *18*(3), 1059. https://doi.org/10.1029/2002PA000777
Lyle, M., & Baldauf, J. (2015). Biogenic sediment regimes in the Neogene equatorial Pacific, IODP Site U1338: Burial, production, and diatom community. *Palaeogeography, Palaeoclimatology, Palaeoecology*, *433*, 106–128.
Martin, H. (2006). Cenozoic climatic change and the development of the arid vegetation in Australia. *Journal of Arid Environments*, *66*(3), 533–563.
Martinez, J. I. (1994). Late Pleistocene palaeocenography of the Tasman Sea: Implications for the dynamics of the warm pool in the western Pacific. *Palaeogeography, Palaeoclimatology, Palaeoecology*, *112*(1–2), 19–62.
Mortimer, N., Campbell, H. J., Tulloch, A. J., King, P. R., Stagpoole, V. M., Wood, R. A., et al. (2017). Zealandia: Earth's hidden continent. *Geological Society of America Today*, *27*(3), 27–35.
Mortimer, N., Gans, P., Meffre, S., Martin, C., Seton, M., Williams, S., et al. (2018). Regional volcanism of northern Zealandia: Post-Gondwana break-up magmatism on an extended, submerged continent. *Geological Society, London, Special Publications*, *463*(1), 199–226.
Mortimer, N., Herzer, R. H., Gans, P. B., Parkinson, D. L., & Seward, D. (1998). Basement geology from three Kings Ridge to West Norfolk Ridge, southwest Pacific Ocean; evidence from petrology, geochemistry and isotopic dating of dredge samples. *Marine Geology*, *148*(3–4), 135–162.
Naish, T., Powell, R., Levy, R., Wilson, G., Scherer, R., Talarico, F., et al. (2009). Obliquity-paced Pliocene West Antarctic ice sheet oscillations. *Nature*, *458*(7236), 322–328. https://doi.org/10.1038/nature07867
Nelson, C. S., Hancock, G. E., & Kamp, P. J. (1982). Shelf to basin, temperate skeletal carbonate sediments, Three Kings Plateau, New Zealand. *Journal of Sedimentary Research*, *52*(3), 717–732.
Oke, P. R., Pilo, G. S., Ridgway, K., Kiss, A., & Rykova, T. (2019). A search for the Tasman Front. *Journal of Marine Systems*, *199*, 103217.
Oke, P. R., Roughan, M., Cetina-Heredia, P., Pilo, G. S., Ridgway, K. R., Rykova, T., et al. (2019). Revisiting the circulation of the East Australian Current: Its path, separation, and eddy field. *Progress in Oceanography*, *176*, 102139.
Orr, D., Sutherland, R., & Stratford, W. (2020). Eocene to Miocene subduction initiation recorded in stratigraphy of Reinga Basin, northwest New Zealand. *Tectonics*, *39*, e2019TC005899. https://doi.org/10.1029/2019TC005899
Pagani, M., Arthur, M. A., & Freeman, K. H. (1999). Miocene evolution of atmospheric carbon dioxide. *Paleoceanography*, *14*(3), 273–292.
Pearson, P. N., & Palmer, M. R. (2000). Atmospheric carbon dioxide concentrations over the past 60 million years. *Nature*, *406*(6797), 695–699.
Rae, J. W. B., Zhang, Y. G., Liu, X., Foster, G. L., Stoll, H. M., & Whiteford, R. D. M. (2021). Atmospheric CO_2 over the past 66 million years from marine archives. *Annual Review of Earth and Planetary Sciences*, *49*(1), 609–641. Retrieved from https://www.annualreviews.org/doi/abs/10.1146/annurev-earth-082420-063026
Rea, D. K., Pisias, N. G., & Newberry, T. (1991). Late Pleistocene paleoclimatology of the central equatorial Pacific: Flux patterns of biogenic sediments. *Paleoceanography*, *6*(2), 227–244.

Ridgway, K., & Dunn, J. (2003). Mesoscale structure of the mean East Australian Current System and its relationship with topography. *Progress in Oceanography*, *56*(2), 189–222.

Rintoul, S., Hughes, C., & Olbers, D. (2001). The Antarctic Circumpolar Current system. In G. Siedler, J. Church, & J. Gould (Eds.), *Ocean circulation and climate* (pp. 271–302). Academic Press.

Royer, D. L., Wing, S. L., Beerling, D. J., Jolley, D. W., Koch, P. L., Hickey, L. J., & Berner, R. A. (2001). Paleobotanical evidence for near present-day levels of atmospheric CO_2 during part of the Tertiary. *Science*, *292*(5525), 2310–2313.

Schellart, W. P., Lister, G. S., & Toy, V. G. (2006). A Late Cretaceous and Cenozoic reconstruction of the southwest Pacific region: Tectonics controlled by subduction and slab rollback processes. *Earth-Science Reviews*, *76*(3–4), 191–233.

Shevenell, A. E., Kennett, J. P., & Lea, D. W. (2004). Middle Miocene southern ocean cooling and Antarctic cryosphere expansion. *Science*, *305*(5691), 1766–1770.

Shevenell, A. E., Kennett, J. P., & Lea, D. W. (2008). Middle Miocene ice sheet dynamics, deep-sea temperatures, and carbon cycling: A Southern Ocean perspective. *Geochemistry, Geophysics, Geosystems*, *9*, Q02006. https://doi.org/10.1029/2007GC001736

Si, W., & Rosenthal, Y. (2019). Reduced continental weathering and marine calcification linked to late Neogene decline in atmospheric CO_2. *Nature Geoscience*, *12*(10), 833–838.

Sosdian, S. M., Greenop, R., Hain, M., Foster, G. L., Pearson, P. N., & Lear, C. H. (2018). Constraining the evolution of Neogene ocean carbonate chemistry using the boron isotope pH proxy. *Earth and Planetary Science Letters*, *498*, 362–376.

Stratford, W. R., Sutherland, R., & Collot, J. (2018). Physical properties and seismic-reflection interpretation of bathyal marine sediments affected by carbonate and silica diagenesis in the Tasman Sea. *New Zealand Journal of Geology and Geophysics*, *61*(1), 96–111.

Sutherland, R. (1999). Basement geology and tectonic development of the greater New Zealand region; an interpretation from regional magnetic data. *Paleomagnetism, Global Tectonics and the Rock Record*, *308*(3), 341–362.

Sutherland, R., Collot, J., Bache, F., Henrys, S., Barker, D., Browne, G. H., et al. (2017). Widespread compression associated with Eocene Tonga-Kermadec subduction initiation. *Geology*, *45*(4), 355–358.

Sutherland, R., Collot, J., Lafoy, Y., Logan, G. A., Hackney, R., Stagpoole, V., et al. (2010). Lithosphere delamination with foundering of lower crust and mantle caused permanent subsidence of New Caledonia Trough and transient uplift of Lord Howe Rise during Eocene and Oligocene initiation of Tonga-Kermadec subduction, western Pacific. *Tectonics*, *29*, TC2004. https://doi.org/10.1029/2009TC002476

Sutherland, R., Dickens, G. R., Blum, P., Agnini, C., Alegret, L., Asatryan, G., et al. (2019). *International Ocean Discovery Program Expedition 371: Tasman Frontier subduction initiation and Paleogene climate* (Vol. 371). International Ocean Discovery Program.

Sutherland, R., Dickens, G. R., Blum, P., Agnini, C., Alegret, L., Asatryan, G., et al. (2020). Continental scale geographic change across Zealandia during Paleogene subduction initiation. *Geology*, *48*, 419–424.

Sutherland, R., Viskovic, G. P. D., Bache, F., Stagpoole, V. M., Collot, J., Rouillard, P., et al. (2012). *Compilation of seismic reflection data from the Tasman Frontier region, southwest Pacific* (Vol. 2012/01). GNS Science.

Van Andel, T. H., Heath, G. R., & Moore, T. C. (1975). Cenozoic history and paleoceanography of the central equatorial pacific ocean a regional synthesis of Deep Sea Drilling Project Data. *Geological Society of America Memoirs*, *143*, 1–223.

Vincent, E., & Berger, W. H. (1985). Carbon dioxide and polar cooling in the Miocene: The Monterey hypothesis. In *The carbon cycle and atmospheric CO2: Natural variations Archean to present* (Vol. 32, pp. 455–468).

Westerhold, T., Marwan, N., Drury, A. J., Liebrand, D., Agnini, C., Anagnostou, E., et al. (2020). An astronomically dated record of Earth's climate and its predictability over the last 66 million years. *Science*, *369*(6509), 1383–1387.

Zachos, J., Pagani, M., Sloan, L., Thomas, E., & Billups, K. (2001). Trends, rhythms, and aberrations in global climate 65 Ma to present. *Science*, *292*(5517), 686–693. Retrieved from http://www.sciencemag.org/cgi/content/abstract/292/5517/686

Zhang, Y. G., Pagani, M., & Liu, Z. (2014). A 12-million-year temperature history of the tropical Pacific Ocean. *Science*, *344*(6179), 84–87.

Zheng, H., Powell, C. M., Rea, D. K., Wang, J., & Wang, P. (2004). Late Miocene and mid-Pliocene enhancement of the East Asian monsoon as viewed from the land and sea. *Global and Planetary Change*, *41*(3–4), 147–155.

Zhisheng, A., Kutzbach, J. E., Prell, W. L., & Porter, S. C. (2001). Evolution of Asian monsoons and phased uplift of the Himalaya–Tibetan plateau since Late Miocene times. *Nature*, *411*(6833), 62–66.